The Dissertation Committee for Benjamin Fonville Garrett certifies that this is the approved version of the following dissertation:

Computational Methods for Understanding the Role of Electric Fields in Quantum Confined Materials

Committee:

James R. Chelikowsky, Supervisor

Alexander A. Demkov

Gregory A. Fiete

Graeme A. Henkelman

Allan H. MacDonald

Computational Methods for Understanding the Role of Electric Fields in Quantum Confined Materials

by

Benjamin Fonville Garrett

Dissertation

Presented to the Faculty of the Graduate School
of the University of Texas at Austin
in Partial Fulfillment
of the Requirements
for the Degree of

Doctor of Philosophy

The University of Texas at Austin
December 2017

Computational Methods for Understanding the Role of Electric Fields in Quantum Confined Materials

Publication No. _____

Benjamin Fonville Garrett, Ph.D.

The University of Texas at Austin, 2017

Supervisor: James R. Chelikowsky

The invention of pseudopotential-density functional theory to solve for the electronic structure of materials is one of the major successes of modern computational physics. A code based on this formalism was used to solve for the electronic structure of systems with limited dimensionality. The code solves for the electronic structure problem on a real-space grid without the use of an explicit basis. This scheme is particularly well suited for studying molecules, clusters, and nanostructures. The code was applied to assess how an applied electric field changes the properties of two different systems: the change of vibrational modes with the field in molecules or clusters and tuning the electronic gap with the field in 2D materials.

Three approaches were employed to study the effect of electric fields on the vibrations of small molecules. The approaches used perturbation theory, a finite field method, and an ab initio molecular dynamics approach. This work provides a better understanding of experimental techniques to probe the local electric field in complex materials as in photovoltaics and biomolecules.

The second part of this thesis leverages mixed boundary conditions to

study the effects of finite electric fields on two-dimensional materials such as phosphorene. These results demonstrate the ability to tune the band gap and drive semiconductor to metallic transitions in novel two-dimensional materials. This property may enable the creation of nanoscale transistors and sensors to power the next generation of electronic devices.

Table of Contents

List of Tables

List of Figures

Chapter 1

Introduction and Background

Confined quantum systems occur when the features of a system approach the same length scale as the wave lengths of the electrons. When this happens, the system can no longer be understood as merely a smaller chunk of a classical bulk material. Instead new behaviors arise as electrons are constrained into smaller regions. The field of nanoscience is charged with understanding the properties of systems so confined in at least one dimension.

The behavior of electrons at the nanoscale is governed by the Schrödinger equation. Unfortunately, for systems with more than one electron, the Schrödinger equation quickly becomes impossible to solve. Electronic structure calculations then require the use of appropriate approximations to the Schrödinger equation. Density functional theory (DFT) with pseudopotentials is one of the most successful and important approximate methods available for ground state electronic structure calculations.

This thesis focuses on a real space implementation of DFT that allows for the efficient study of confined systems under electronic fields. The first application examines how electronic fields affect the vibrational properties of molecules. Understanding this relationship can give new tools to understand electric fields at the nanoscale. The second application looks at the effects of electric fields on new 2D semiconductors. The ability to tune these 2D semiconductors opens doors to molecular scale transistors and sensors.

1.1 Theoretical Background

1.1.1 The Kohn-Sham Equations

The central problem in electronic structure calculations is to find the energy and spatial distributions of electrons in matter. These wave functions are the eigenvalues of a Schrödinger equation (1.1).

$$\hat{H}\psi = E\psi \tag{1.1}$$

If we take the Born-Oppenheimer approximation as a given, that is, fix the nuclear coordinates while solving the electronic problem, we can break up the Hamilton operator $\hat{H}$ into four terms:

$$\hat{H} = \hat{T}_e + \hat{V}_{ion-e} + \hat{V}_{e-e} + E_{ion-ion} \tag{1.2}$$

$\hat{T}_e$ represents the kinetic energy of the electrons, $\hat{V}_{ion-e}$ is the potential energy between nuclei and electrons, $\hat{V}_{e-e}$ is the Coulombic interaction between electrons, and $E_{ion-ion}$ is a classical term for the repulsion between nuclei. In a system with n electrons with coordinates $\mathbf{r}_i$ and N nuclei with coordinates

$\mathbf{R}_I$ and nuclear charges Z_I, these operators take the form:

$$\begin{aligned}
\hat{T}_e &= -\frac{\hbar^2}{2m_e}\sum_{i=1}^{N_e}\nabla_i^2 \\
\hat{V}_{ion-e} &= -\sum_{i=1}^{N_e}\sum_{I=1}^{N_{ion}}\frac{Z_I e^2}{|\mathbf{r}_i - \mathbf{R}_I|} \\
\hat{V}_{e-e} &= \sum_{j=i+1}^{N_e}\sum_{i=1}^{N_e-1}\frac{e^2}{|\mathbf{r}_i - \mathbf{r}_j|} \\
E_{ion-ion} &= \sum_{J=I+1}^{N_{ion}}\sum_{I=1}^{N_{ion}-1}\frac{Z_J Z_I e^2}{|\mathbf{R}_J - \mathbf{R}_I|}
\end{aligned} \tag{1.3}$$

where m_e is the mass of an electron, $\mathbf{r}_i$ is the coordinate for the i^{th} electron, and $\mathbf{R}_I$ is the coordinate for the I^{th} nucleus.

When $N_e = N_{ion} = 1$, that is to say there is only one electron and one nucleus, the $\hat{V}_{e-e}$ term disappears and an analytic solution is possible, yielding hydrogen like orbitals. However, the addition of one more electron such that $N_e = 2$ yields no closed form solutions. With the divergence of the Coulomb potential and exploding dimensionality, even numerical methods become impractical for directly solving the basic Schrödinger equation in small molecules and infeasible for large molecules or complex crystalline matter. For much of the last century, the field of condensed matter physics has been concerned with how to develop approximations to the Schrödinger equation that make the problem tractable, while producing physically meaningful results.

The key observation from Hohenberg and Kohn that makes density functional theory (DFT) possible, is that while the wave function ψ corresponding to any given ionic potential is a complicated 3n dimensional object

with spin, the much simpler charge density $n(\mathbf{r})$ must necessarily contain all observable information about the system. This must be so since for a particular number of electrons, there is a one-to-one correspondence between densities $n(\mathbf{r})$ and external potential $V_{ion}(\mathbf{r})$. Thus, we can write the total energy in terms of functionals of the charge density:

$$E[n] = T[n] + V[n] + U[n] \tag{1.4}$$

where $T[n]$ is the kinetic energy, $V[n]$ is the interaction energy between electrons and ions (or any other external potential), and $U[n]$ is the interaction energy between electrons. Hohenberg and Kohn also showed that the density $n(\mathbf{r})$ that minimizes $E[n]$ is the ground state density for the physical system. To turn this into a practical method Kohn and Sham suggested introducing a non-interacting system of normalized wave functions $\phi_i(\mathbf{r})$. These wave functions are related to the density by:

$$n(\mathbf{r}) = \sum_{i=1}^{N_e} \phi_i^2(\mathbf{r}) \tag{1.5}$$

The kinetic energy term for this system T_s is then:

$$T_s = -\frac{\hbar^2}{2m_e} \sum_{i=1}^{N_e} \langle \phi_i | \nabla^2 | \phi_i \rangle \tag{1.6}$$

The effective functional for the external potential is relatively easy to compute:

$$V[n] = \int V_{ion}(\mathbf{r}) n(\mathbf{r}) d\mathbf{r} \tag{1.7}$$

The electron interaction functional, however, proves more difficult. One step is to split this term into the known expression for a Coulombic interaction and group the nonclassical parts into what is known as the exchange-correlation functional $E_{XC}[n]$:

$$U[n] = \frac{1}{2}\int \frac{n(\mathbf{r}_1)n(\mathbf{r}_2)}{|\mathbf{r}_1 - \mathbf{r}_2|} d\mathbf{r}_1 d\mathbf{r}_2 + E_{XC}[n] \tag{1.8}$$

If we allow $E_{XC}[n]$ to also absorb the difference between the true kinetic energy functional $T[n]$ and the kinetic energy of the reference system T_s, then we can rewrite (1.4) as:

$$\begin{aligned} E[n] = &- \frac{\hbar^2}{2m_e}\sum_{i=1}^{N_e} \langle \phi_i | \nabla^2 | \phi_i \rangle + \int V_{ion}(\mathbf{r}) n(\mathbf{r}) d\mathbf{r} \\ &+ \frac{1}{2}\int \frac{n(\mathbf{r}_1)n(\mathbf{r}_2)}{|\mathbf{r}_1 - \mathbf{r}_2|} d\mathbf{r}_1 d\mathbf{r}_2 + E_{XC}[n] \end{aligned} \tag{1.9}$$

Applying the variational principle to this functional allows us to find the conditions under which the non-interacting wave functions ϕ_i produce the ground state energy. The resulting constraints are known as the Kohn-Sham equations [5]:

$$\left(-\frac{1}{2}\nabla^2 + V_{ion}(\mathbf{r}) + V_H(\mathbf{r}) + V_{XC}(\mathbf{r})\right)\phi_i = \varepsilon_i \phi_i \tag{1.10}$$

where the Hartree Potential V_H and exchange-correlation potential V_{XC} are given by:

$$V_H(\mathbf{r}) = \int \frac{n(\mathbf{r}')}{|\mathbf{r} - \mathbf{r}'|} d\mathbf{r}' \tag{1.11}$$

$$V_{XC} = \frac{\delta E_{XC}[n]}{\delta n} \tag{1.12}$$

While the expression 1.11 is sufficient to define V_H, performing such an integral for every grid point is inefficient. In practice the Hartree potential is found as the solution to the Poisson equation:

$$\nabla^2 V_H(\mathbf{r}) = -4\pi n(\mathbf{r}) \tag{1.13}$$

This form can be solved by the conjugate gradient method in conjunction with appropriate boundary conditions [6].

One important feature of (1.10) is that both V_H and V_{XC} are dependent on the charge density n which is in turn related to the wave functions ϕ_i by (1.5). In practice this means the Kohn-Sham equations must be solved iteratively using a self-consistent field (SCF) method. First, the total charge density of the system can be approximated by the summed charge densities of the individual atoms. This density estimate then determines initial approximations of the Hartree and exchange-correlation potentials. Using approximate V_H and V_{XC}, (1.10) is solved as an eigenvalue problem for the lowest energy wave functions. The set of wave functions ϕ_i then yields a new charge density via (1.5). At this point the sequence can cycle as $n(\mathbf{r}) \rightarrow \{V_H, V_{XC}\} \rightarrow \{\phi_i\} \rightarrow n(\mathbf{r})$, known as the SCF loop. The loop exits when the residual change in the density $n(\mathbf{r})$ or the potentials V_H, V_{XC} falls below a threshold value.

1.1.2 The Local Density Approximation

The development of DFT as cast is exact. With an appropriate expression for $E_{XC}[n]$, the Kohn-Sham equations (1.10) would yield the true ground

state density n (although even in this exact scenario, the reference states ϕ_i are not necessarily physically meaningful). Unfortunately, however, no such expression exists, and if it did, there is no guarantee its evaluation would be less computationally demanding than solving the Schrödinger equation directly. Therefore, making DFT a computationally useful method involves finding approximate expressions for the exchange-correlation functional.

The simplest useful approximation is known as the local density approximation (LDA). This method assumes the contribution to the total exchange-correlation energy from each point in space is only due to the charge density at that particular point (i.e. there are no non-local contributions). This allows us to write:

$$E_{XC}^{LDA}[n] = \int n(\mathbf{r})\epsilon_{XC}(\mathbf{r})d\mathbf{r} \tag{1.14}$$

Bloch and Dirac showed that for a homogeneous electron gas, the exchange part of this expression can be written analytically:

$$\epsilon_X = -\frac{3}{4}\left(\frac{3n(\mathbf{r})}{\pi}\right)^{\frac{1}{3}} \tag{1.15}$$

Unfortunately there is no simple corresponding expression for the correlation component. At this point LDA functionals typically make use of data from quantum Monte Carlo methods as from the work of Ceperley and Alder [7].

Despite the simplicity of the approximation, LDA is remarkably useful in calculating the ground state properties of molecules and solids. Bond lengths are typically accurate within 2%. Vibrational frequencies are likewise generally

accurate to within a few percent. The computational efficiency of LDA and absence of tunable parameters make LDA a standard approach for *ab initio* calculations.

1.1.3 The Pseudopotential Method

While the Kohn-Sham equations coupled with an appropriate approximation for the exchange-correlation potential make DFT tractable by replacing a system of interacting electrons in a high dimensional wave function with a set of non-interacting three-dimensional orbitals, numerical methods are still challenged by the singularity of the Coulomb potential. The depth of the potential means that core electrons experience disparate length and energy scales from the outermost valence electrons. For example, the binding energy of a 1s electron in Germanium is of the order 11,000 eV, while the outermost electrons are only bound by less than 10 eV [8]. The core electrons also add considerably to the number of eigenstates of the Kohn-Sham equations that must be found. Even for a moderate atomic weight element such as Silicon, 10 out of 14 electrons are core electrons unaffected by normal bonding and structural considerations. Avoiding a direct calculation of these states reduces the number of orbitals needed by over 70%. As most eigenvalue algorithms scale like $\mathcal{O}(N^3)$ for N eigenvalues, this translates into a dramatic reduction in computational expense.

At long ranges, pseudopotentials are simply the effective Coulomb potential for the combination of nuclear and core electron charges. Near the core, however, more careful modifications are needed to address the steep sloped po-

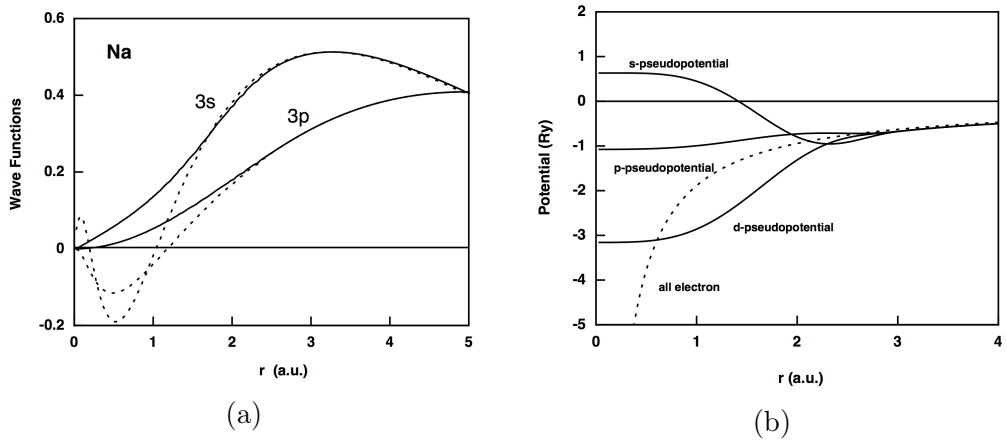

(a) (b)

Figure 1.1: (a) Pseudo wave functions and (b) pseudopotentials for a sodium atom [2].

tential and highly oscillatory wave functions. The general method to construct a pseudopotential is to first solve the all electron problem for an isolated atom using DFT and the desired exchange-correlation functional. The valence wave functions for the atomic system are then used construct new pseudo wave functions with more desirable properties. The general strategy is to have the pseudo wave function match the all-electron wave function exactly outside of a chosen cutoff radius r_c. Inside the cutoff radius, however, the pseudo wave function is designed to smoothly approach the origin without nodes. Once an appropriate pseudo wave function is chosen, it is replaced back into the Kohn-Sham equations, which are then reversed to solve for the pseudopotential that would have generated it. Figure 1.1 provides examples of the pseudo wave function and pseudopotentials for a sodium atom.

In this work we make use of the formulation described by Troullier-Martins [9] to construct our pseudopotentials. They give the following form

for the pseudo wave function inside of r_c:

$$\begin{aligned} \phi_p(r) =& r^l e^{p(r)} \quad \text{for} \quad r < r_c \\ p(r) =& \sum_{n=0}^{6} c_{2n} r^{2n} \end{aligned} \tag{1.16}$$

The seven coefficients c_{2n} are then found by ensuring: (i) the norm of the wave function is conserved (ii) the pseudopotential has zero curvature at the origin and (iii) the pseudo wave function and its first four derivatives are continuous with the all electron wave function at r_c.

1.1.4 Real Space Methods

There are several numerical methods available to solve the Kohn-Sham equations (1.10). A common method makes use of a plane wave basis set. These have the form:

$$\phi_{\mathbf{k}}(\mathbf{r}) = \sum_{\mathbf{G}} \alpha(\mathbf{k}, \mathbf{G}) \exp(i(\mathbf{k} + \mathbf{G}) \cdot \mathbf{r}) \tag{1.17}$$

where $\mathbf{k}$ is the wave vector, $\mathbf{G}$, and $\alpha(\mathbf{k}, \mathbf{G})$ are the coefficients for the basis. One advantage of this method is that it diagonalizes the Laplacian term of the Hamiltonian. It is also naturally suited to periodic systems where $\mathbf{k}$ is a well defined quantum number. However, systems which are not fully periodic such as isolated molecules or 2D materials must make use of a large super-cell to avoid the system interacting with periodic images of itself. Calculating the charge density self-consistently with plane waves also involves repeatedly calculating fast Fourier Transforms (FFTs). FFTs require large amounts of

communication, making them less suited to massively parallel computing environments. [2]

Alternatively, we can represent the wave function in real space as a vector taking values on a cubic set of grid points (x_i, y_j, z_k). Higher order finite differencing is then used to find the Laplacian. In this scheme, the second derivative $\partial^2\phi/\partial x^2$ evaluated at point (x_i, y_j, z_k) is approximated by:

$$\frac{\partial^2\phi}{\partial x^2} = \sum_{n=-M}^{M} C_n \phi(x_i + nh, y_j, z_k) + \mathrm{O}(h^{2M+2}) \tag{1.18}$$

where h is the grid spacing, M is the order of the finite differencing, and C_n are the coefficients of the finite differencing scheme. The matrix form of the Hamiltonian can then be written:

$$\begin{aligned}\hat{H} =& \frac{-\hbar^2}{2m}\left\{\sum_{n_1=-M}^{M} C_{n_1}\phi(x_i + n_1 h, y_j, z_k) + \sum_{n_2=-M}^{M} C_{n_2}\phi(x_i, y_j + n_2 h, z_k)\right. \\ &\left. + \sum_{n_3=-M}^{M} C_{n_3}\phi(x_i, y_j, z_k + n_3 h)\right\} + V_{ion}(x_i, y_j, z_k) + V_H(x_i, y_j, z_k) \\ &+ V_{XC}(x_i, y_j, z_k)\end{aligned} \tag{1.19}$$

While an explicit representation of this matrix might be quite large, $n \times n$ for a set of n grid points, the matrix is exceedingly sparse and need not be stored explicitly. V_H and V_{XC} are diagonal while the Laplacian depends on a stencil that introduces a few off diagonal terms. The all electron ionic potential is local and diagonal. One disadvantage of replacing it with a pseudopotential is that the pseudopotential contains non-local components. Fortunately, the

non-local form can still be efficiently represented in the Kleinman-Bylander form [10] as:

$$V_{ion}^{p} = \sum_{a} V_{loc,a} + \sum_{a,l,m} c_{a,l,m} U_{a,l,m} U_{a,l,m}^{T} \tag{1.20}$$

where a sums over atomic sites and l and m are the quantum numbers for atomic orbitals. The vectors $U_{a,l,m}$ are sparse and zero outside of the cutoff radius of each atom, and $c_{a,l,m}$ are associated normalization coefficients. Figure 1.2 illustrates the structure of this matrix for a $Ge_{99}H_{100}$ nanocluster where less than 0.1% of grid points are nonzero.

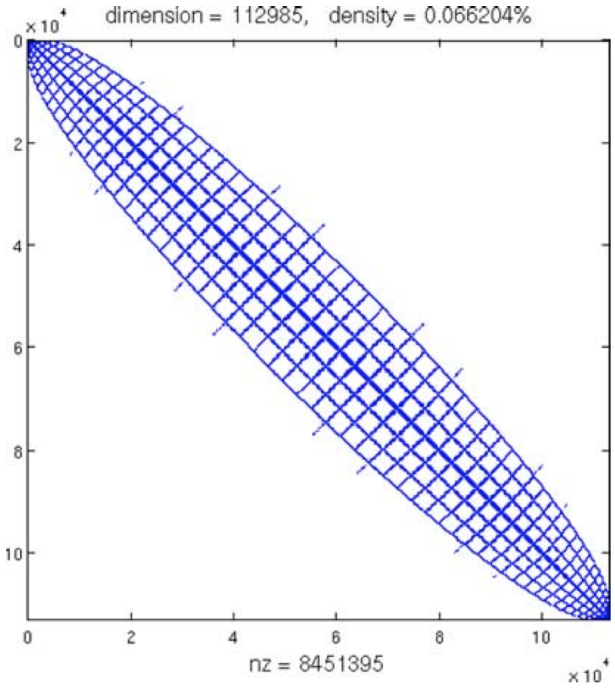

Figure 1.2: Visualization of the sparse matrix representation of the Hamiltonian for $Ge_{99}H_{100}$ [2].

While this matrix often has many more elements than a comparable plane wave method, the sparsity and near-locality make it well suited to mod-

ern parallel computing environments that place a premium on global communication.

1.1.5 Chebyshev Filtering

The Kohn-Sham equations (1.10) must be solved self-consistently, i.e. the potentials V_H and V_{XC} must agree with the density produced by the wave functions ϕ_i. In practice this means we solve (1.10) iteratively. Diagonalizing the Hamiltonian is the most expensive step of this iteration. To reduce the time spent finding eigenvalues, Zhou *et al.* proposed a Chebyshev-filtered subspace iteration technique (CheFSI) [11].

The CheFSI method starts with an approximate diagonalization of the initial estimate of the Hamiltonian. This provides estimates for the range of energies and the subspace spanned by the occupied orbitals. Since the number of possible eigenvalues corresponds to the number of grid points while the number of occupied orbitals is only half the number of electrons, working in this subspace vastly reduces the cost of orthogonalizations compared to any naive approach. Critically, knowledge of the subspace spanned by the occupied states allows one to compute the total charge density even if the individual wave functions are not known exactly. This can be seen from the simple observation that if the Φ is a matrix of the occupied eigenvectors, the charge density at each grid point is found along the main diagonal of $\Phi\Phi^{\mathrm{T}}$. If $\tilde{\Phi}$ is a different set of orthonormal vectors spanning the same subspace, there exists an orthogonal matrix $\mathcal{Q}$ such that $\tilde{\Phi} = \Phi\mathcal{Q}$. Then by orthogonality we have $\tilde{\Phi}\tilde{\Phi}^{\mathrm{T}} = (\Phi\mathcal{Q})(\Phi\mathcal{Q})^{\mathrm{T}} = \Phi\Phi^{\mathrm{T}}$ and find identical charge densities independent of

basis set. At every SCF iteration after the first, the CheFSI method does not find exact eigenvalues and eigenvectors, but rather attempts to improve the estimate of the subspace via filtering.

Filtering the subspace is achieved via the use of Chebyshev polynomials of the Hamiltonian. Chebyshev polynomials radically suppress values in the range $[-1, 1]$. If the lowest eigenvalue is ε_0, the highest occupied is ε_{occ}, and highest unoccupied is ε_{max}, then a coordinate shift is performed to map the range $[-1, 1]$ onto $[\varepsilon_{occ}, \varepsilon_{max}]$. For an arbitrary order, the corresponding Chebyshev polynomial is generated with the recurrence relation:

$$\begin{aligned} C_0(t) =& 1 \\ C_1(t) =& t \\ C_{k+1}(t) =& 2tC_k(t) - C_{k-1}(t) \end{aligned} \tag{1.21}$$

With this recursion relation, each SCF iteration builds a Chebyshev filter from the current estimate of the Hamiltonian, applies the filter to the existing subspace estimate, then calculates the charge density from the subspace. The structure of the algorithm is summarized in Figure 1.3. While self-consistency requires approximately the same number of iterations as diagonalization based methods, each iteration (after the first) is significantly less costly. Once self-consistency is achieved, explicit eigenvectors can be obtained by Rayleigh-Ritz refinement. Numerical tests show the CheFSI method can produce speedups of an order of magnitude or more, significantly increasing the size or number of systems that can be practically worked on [11–13].

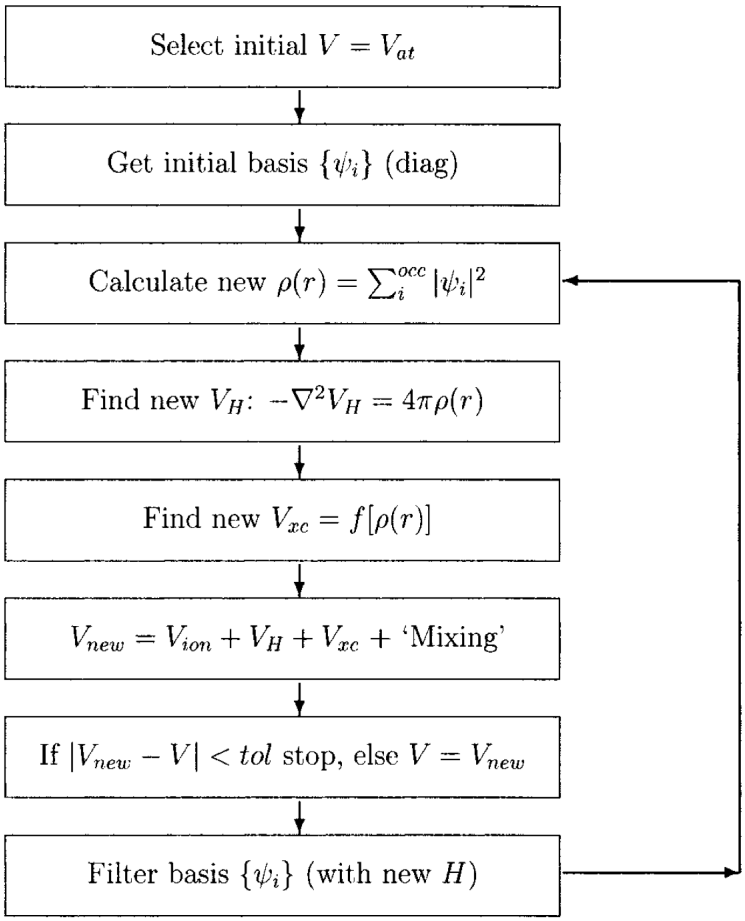

Figure 1.3: Schematic of the SCF loop in the CheFSI method [3].

.

1.2 Applying the real-space method to confined systems

The real-space formulation of DFT can be readily applied to confined systems under external fields. With the current state and scope of computational methods and resources, almost any single electronic structure problem can be solved with enough resources. However, with the even greater breadth of systems worth investigating, efficient and meaningful progress can only be made by intelligent application of techniques to the systems they are suited

for.

1.2.1 Boundary Conditions

In contrast to basis function methods such as the plane waves discussed in section 1.1.4, solving the Kohn-Sham equations on a discrete grid imposes no prior conditions on the nature of the space under study. Molecules and nanoclusters are not periodic in any direction and hence are naturally represented in 0D or cluster boundary conditions. It is in this case the implementation of the matrix form (1.19) is most straightforward. As illustrated in Figure 1.4, a spherical domain is chosen with a given radius centered on the system of interest. (Although the domain is spherical, the grid points within the domain remain on a cubic grid to preserve the symmetry and simplicity of the Laplacian stencil.) The wave functions are allowed to take any values on grid points within the domain, but must vanish at the boundary. As electron orbitals decay exponentially, it does not take a great bounding radius to ensure this constraint does not impinge on the accuracy of calculated wave functions.

Introducing periodic symmetry does not require much more work than simply identifying grid points at one end with the other and adjusting the Laplacian stencil to match. The periodic systems of interest to us will be two dimensional. Consider an orthorhombic 2D system as illustrated in Figure 1.5. The x and y axes are periodic with cell lengths a and b respectively. The z axis, however, is non-periodic and confined to domain of span of L. As in the case of cluster boundary conditions, we require that the wave functions vanish at $z = \pm L/2$. We make use of Bloch's theorem to write the wave functions in

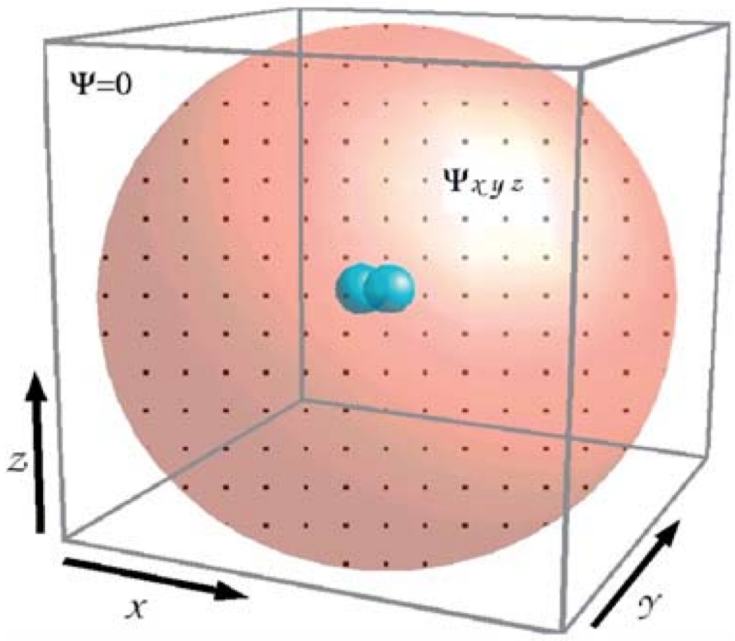

Figure 1.4: Grid structure and boundary conditions for cluster (0D) boundary conditions [4].

terms of a plane wave and periodic functions u:

$$\begin{aligned} \phi_{n,\mathbf{k}}(\mathbf{r}) =& e^{i\mathbf{k}\cdot\mathbf{r}} u_{n,\mathbf{k}}(\mathbf{r}) \\ u_{n,\mathbf{k}}(\mathbf{r} + n_1 a\hat{x} + n_2 b\hat{y}) =& u_{n,\mathbf{k}}(\mathbf{r}) \quad \forall \ \{n_1, n_2\} \in \mathbb{Z} \end{aligned} \tag{1.22}$$

where instead of labeling a discrete wave function, n now indicates the band index and $\mathbf{k}$ is a wave vector. To maintain the well defined dot product $\mathbf{k}\cdot\mathbf{r}$, $\mathbf{k}$ can be written as a three dimensional vector whose z component is zero. The second line of (1.22) is simply the constraint that the function $u_{n,\mathbf{k}}$ is periodic along the x and y axes in a cell with lengths a and b. If we substitute the expression for $\phi_{n,\mathbf{k}}$ into the Kohn-Sham equations (1.10), we find the modified

equations for $u_{n,\mathbf{k}}$:

$$\left(-\frac{1}{2}\left(\nabla^2 + 2i\mathbf{k}\cdot\nabla - \mathbf{k}^2\right) + V_{eff}(\mathbf{r})\right) u_{n,\mathbf{k}} = \varepsilon_{n,\mathbf{k}} u_{n,\mathbf{k}} \tag{1.23}$$

where V_{eff} is simply the sum of V_H, V_{ion}, and V_{XC}. The charge density is then found by integrating over all possible $\mathbf{k}$ in the Brillouin zone:

$$n(\mathbf{r}) = \int_{BZ} \sum_{n=1}^{N_{occ}} |u_{n,\mathbf{k}}(\mathbf{r})|^2 \tag{1.24}$$

In practice, of course, we do not wish to solve (1.23) and (1.24) for an infinite number of $\mathbf{k}$ vectors. Instead the irreducible Brillouin zone is sampled with a discrete set of points, arranged in a mesh as detailed by Monkhorst and Pack [14]. This allows the integral in (1.24) to be evaluated as a sum. Convergence of the density then requires a sufficient sampling of $\mathbf{k}$ points in the Brillouin zone.

An additional consideration for periodic boundary conditions is the calculation of the ionic potential across neighboring unit cells. Because the ionic potential drops off as $1/r$ while the number of nuclei at given distance grows linearly with distance in a 2D system, a simple summation of the ionic potentials will not converge. This is not a problem in real uncharged crystals because an electron never experiences the unscreened nuclear potential – the potential due to other electrons balances the nuclear potential at long range. We address this using an Ewald-like sum to balance the long range interactions [15]. A compensating charge with a Gaussian distribution is placed at every nucleus such that the sum over periodic images does not diverge and V_{ion} can

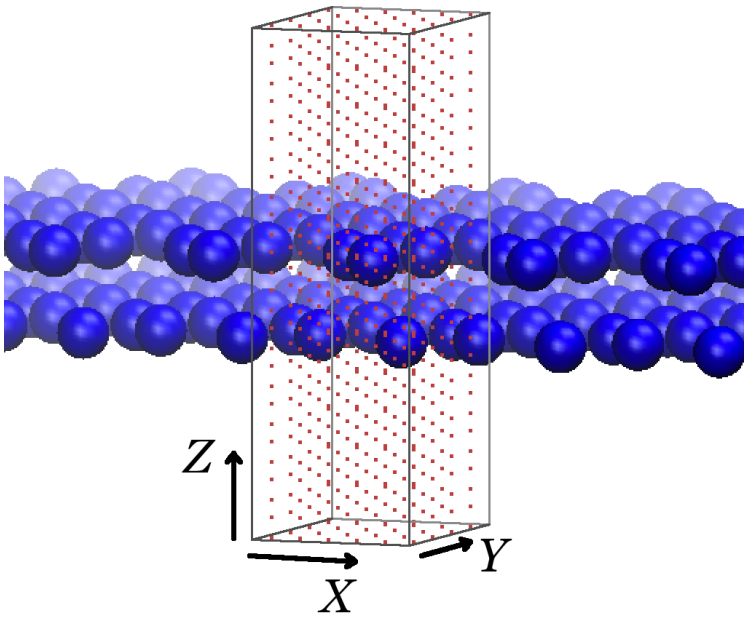

Figure 1.5: Grid structure and boundary conditions for slab (2D) boundary conditions.

be calculated. To maintain a neutral system, the opposite Gaussian charge distribution is included in the density used to calculate the Hartree potential V_H. Since V_{ion} and V_H and summed in the Hamiltonian, the effect is as if there was no added charge, while making it possible to calculate the two terms independently.

1.2.2 Applied Electric Fields

The ability to employ non-periodic boundary conditions also gives the opportunity to efficiently explore the effect of large applied electric fields to these confined systems. In a plane wave basis paradigm, the potentials are

also defined in momentum space and inherently periodic. An electric field, however, produces a linear potential, which is non-periodic. This can be handled for confined systems by modifying the field's potential into a sawtooth pattern, where the potential resets far away from the charge carrying regions, but this requires additional vacuum space in the system. Alternatively, dielectric properties can be evaluated with perturbation theory and mixed-space coordinates, which requires many additional states be calculated, reducing performance [16]. DFT based on basis set functions is suited to non-periodic boundary conditions. However, accounting for an electric field requires the addition of polarization functions to the basis set. [17, 18]

In real space DFT, there is no requirement that potentials be periodic, and the representation of a finite field is trivial. In the absence of an explicit basis, the polarization of a wave function is represented by the shifting of charge from one grid point to the next. The modified Kohn Sham equations take the form:

$$\left(-\frac{1}{2}\nabla^2 + V_{eff}(\mathbf{r}) - \mathbf{F}\cdot\mathbf{r}\right)\phi_i(\mathbf{r}) = \varepsilon_i\phi_i(\mathbf{r}) \tag{1.25}$$

where V_{eff} is the sum of V_{ion}, V_H, and V_{XC}, and $\mathbf{F}$ is the desired applied field. As this new potential term is purely local it only affects the main diagonal of the Hamiltonian matrix, maintaining the numerical properties discussed in Section 1.1.4. In practice, V_H and V_{XC} must be recalculated many times as part of the SCF loop, while V_{ion} remains static. For this reason, the electric potential $-\mathbf{F}\cdot\mathbf{r}$ is simply included as a modification of the ionic potential.

Chapter 2

The Vibrational Stark Effect

The application of a static electric field can alter the vibrational modes in clusters, molecules, and condensed matter. Known as the "vibrational Stark effect," this can be an important tool for extracting information on the electrostatic environments at the atomic scale. In particular, the change in the frequency of a vibrational mode with an applied field can be understood by the Stark tuning rate, $\Delta\mu$, which quantifies how much an applied electric field will shift the vibrational frequencies. Knowing $\Delta\mu$ for a probe molecule allows one to use spectroscopy to determine the local electric fields the probe is subjected to, which may otherwise be unmeasurable.

The tuning rate is obtained by a knowledge of the field and the observed change in frequency:

$$hc\Delta\tilde{\nu}_{obs} = -\Delta\vec{\mu}_{probe} \cdot \vec{F}_{environment} \tag{2.1}$$

Here $\Delta\tilde{\nu}_{obs}$ is an observed change in vibrational wave number, $\Delta\vec{\mu}_{probe}$ is the tuning rate for a given molecule and vibrational mode, and $\vec{F}_{environment}$ is the electric field the probe molecule is exposed to. The effect is linear in field strength, and the dot product accounts for orientation of the field and mode.

In biological systems, this technique is being used to measure the fields generated inside of proteins and nucleic acids by incorporating nitrile probes into the target molecules [19–24]. In interface science, surface enhanced spec-

troscopy of self-assembled monolayers on electrodes sheds light on the interfacial potential distribution where local fields may reach 10^7 V/cm. [25–27]

Accurate *ab initio* calculations of the Stark tuning rate have proven challenging. [28] Even for a simple probe molecule such as CO, experimental results vary from 0.43 to 0.67 $cm^{-1}/(MV/cm)$ [23,29,30] while reported calculations have been more consistent, ranging from 0.47 to 0.51 $cm^{-1}/(MV/cm)$ [1, 31]. However, literature calculations for even modestly more complex molecules such as acetone show larger reported differences, ranging from 0.58 to 0.69 $cm^{-1}/(MV/cm)$. [1,23,30–32]

The first difficulty in computing the Stark shift is simply the scale of the effect. A typical probe molecule may have a stretching frequency of roughly 2000 cm^{-1}, which density functional theory can calculate with errors of a few percent using standard approximations. An applied field of 1 MV/cm would perturb this frequency by less than 1 cm^{-1}. Thus, to even detect these frequency shifts the convergence must be controlled much more carefully than for vibrational analysis. DFT using basis set methods must include additional polarization functions to account for the effect of the external fields. As nuclear coordinates and applied fields vary, this makes ensuring convergence nontrivial. Convergence of plane wave methods is more directly accounted for by the cutoff energy, but the artificial periodicity introduced by these methods complicates the study of single molecules. Sufficiently large vacuum spaces must be introduced to prevent dipoles from interacting with their fictitious neighbors. Compensating background charges must be added in the case of charged species, such as CN^-, so that the molecule is not residing in a sea of

infinite charge. In light of these factors, we make use of real space methods, where convergence is controlled by a single parameter, the grid spacing h, but non-periodic boundary conditions are readily implemented, allowing for the natural introduction of charged species and finite applied fields. [17, 18]

From a theoretical perspective, a naive harmonic analysis of the vibrational modes may underestimate the size of the tuning rate by an order of magnitude. For example, with a diatomic such as CO, the vibrational potential $U(q)$ is perturbed by the product of the dipole moment and the field $\vec{\mu}(q) \cdot \vec{F}$. Assuming the vibrational potential is quadratic in coordinate q and Taylor expanding the dipole moment, the constant term $\vec{\mu}(0)$ only changes the total energy. The linear term $\partial\vec{\mu}/\partial q$ shifts the equilibrium bond length but not the frequency. The quadratic term $\partial^2\vec{\mu}/\partial q^2$ does change the effective spring constant and hence causes a frequency shift, but this explains less than 10% of the tuning rate. As DFT calculations of vibrational modes typically make use of the implicitly harmonic dynamical matrix, this raises concerns that subtle anharmonic interactions may be missed. We make use of parallel approaches with and without the dynamical matrix to address these concerns. Our perturbative results illustrate that the coupling of the linear dipole response, $\partial\vec{\mu}/\partial q$, to anharmonicities in the vibrational potential $U(q)$ is responsible for the majority of the change in frequency.[1]

[1]Portions of this chapter have been published as a journal article. [33]
Author contributions: Garrett – developed methods, performed calculations, and wrote manuscript; Azuri and Kronik – verified initial results with an all-electron code; Chelikowsky – supervised project.

2.1 Perturbative Analysis of the Vibrational Stark Effect

While the vibrational Stark effect is useful for probing electric fields that appear quite large at the macroscale, at the atomic scale these fields are comparatively weak. For example, reported field strengths are often in the range 1–10 MV/cm [20,22] which is of the same order as the dielectric strength for many insulators. In comparison, the electric field experienced by an electron one Bohr radius from a hydrogen nucleus is approximately 5000 MV/cm. Thus, from the perspective of an electronic structure calculation, external fields represent only a minor change to the Hamiltonian. This suggest perturbative approximations to the change in total energy are valid. Further, the tuning rate is in fact defined in the limit of a vanishing field. From these facts we first seek to develop perturbative expressions for the tuning rate that can be evaluated from field-free DFT calculations.

2.1.1 Theory

We begin with the total electronic energy for a given nuclear coordinates as the potential energy for the vibrational problem $V(\vec{R})$. Assuming we choose our coordinate system such that $\vec{R} = 0$ is a local minimum, we can Taylor expand this potential to find:

$$V(\vec{R}) = V(0) + \frac{1}{2} \left.\frac{\partial^2 V}{\partial R_i \partial R_j}\right|_{\vec{R}=0} R_i R_j + \frac{1}{6} \left.\frac{\partial^3 V}{\partial R_i \partial R_j \partial R_k}\right|_{\vec{R}=0} R_i R_j R_k \qquad (2.2)$$

To reduce the problem to a single dimension, we diagonalize the stan-

dard dynamical matrix to find the vibrational modes $\vec{q_i}$.

$$D_{ij} = \frac{1}{\sqrt{M_i M_j}} \frac{\partial^2 V}{\partial R_i \partial R_j} \tag{2.3}$$

$$D\vec{q_i} = \lambda_i \vec{q_i} \tag{2.4}$$

For a given mode $\vec{q}$, the single dimensional vibrational potential then takes the form:

$$\begin{aligned} V_q(x) = V(x\vec{q}) =& V(0) + \frac{1}{2} \left. \frac{\partial^2 V}{\partial R_i \partial R_j} \right|_{\vec{R}=0} q_i q_j x^2 \\ &+ \frac{1}{6} \left. \frac{\partial^3 V}{\partial R_i \partial R_j \partial R_k} \right|_{\vec{R}=0} q_i q_j q_k x^3 \end{aligned} \tag{2.5}$$

We can now fit the terms of this potential to the textbook case of a harmonic oscillator with effective mass M and a perturbing cubic anharmonicity of magnitude A.

$$H(x) = \frac{p^2}{2M} + \frac{M\omega^2}{2} x^2 + Ax^3 \tag{2.6}$$

We make use of the traditional treatment of a harmonic Hamiltonian $H_0(x) = \frac{p^2}{2M} + \frac{M\omega^2}{2} x^2$ with eigenstates $|n\rangle$ and energies $E_n^{(0)} = \hbar\omega(n + \frac{1}{2})$. The anharmonic vibrational Hamilton is then $H(x) = H_0(x) + V(x)$ where $V(x) = Ax^3$. Perturbation theory to first order yields a corrected energy given by:

$$E_n^{(1)} = \langle n | V | n \rangle = A \langle n | x^3 | n \rangle \tag{2.7}$$

For the cubic anharmonicity shown, this correction is identically zero. We

consider the second order energy correction given by:

$$E_n^{(2)} = \sum_{m \neq n} \frac{\left|\langle m| V |n\rangle\right|^2}{E_n^{(0)} - E_m^{(0)}} = A^2 \sum_{m \neq n} \frac{\left|\langle m| x^3 |n\rangle\right|^2}{E_n^{(0)} - E_m^{(0)}} \tag{2.8}$$

This expression can be evaluated using the textbook treatment of ladder operators defined by:

$$\begin{gathered} a = \sqrt{\frac{M\omega}{2\hbar}} \left(q + i\frac{p}{M\omega}\right), a^\dagger = \sqrt{\frac{M\omega}{2\hbar}} \left(q - i\frac{p}{M\omega}\right) \\ q = \sqrt{\frac{\hbar}{2M\omega}} \left(a^\dagger + a\right), p = i\sqrt{\frac{\hbar}{2M\omega}} \left(a^\dagger - a\right) \end{gathered} \tag{2.9}$$

Substituting the ladder operators and expressions for $E_n^{(0)}$ into (2.8) yields:

$$E_n^{(2)} = \frac{\hbar^2 A^2}{8M^3\omega^4} \sum_{m \neq n} \frac{\left|\langle m| (a^\dagger + a)^3 |n\rangle\right|^2}{n - m} \tag{2.10}$$

This expression can be straightforwardly evaluated for the two lowest vibrational states using the textbook action of ladder operators on eigenstates of the harmonic oscillator, that is $a^\dagger |n\rangle = \sqrt{n+1}\,|n+1\rangle$ and $a\,|n\rangle = \sqrt{n}\,|n-1\rangle$. The perturbed vibrational energy levels are thus given by:

$$\begin{aligned} E_0 + E_0^{(2)} &= \frac{\hbar\omega}{2} - \frac{11\hbar^2 A^2}{8M^3\omega^4} \\ E_1 + E_1^{(2)} &= \frac{3\hbar\omega}{2} - \frac{71\hbar^2 A^2}{8M^3\omega^4} \end{aligned} \tag{2.11}$$

As the observable quantity in spectroscopy is the energy difference between states, we calculate $E_1 + E_1^{(2)} - E_0 - E_0^{(2)}$ from (2.11) to find the fun-

damental transition energy:

$$\nu = \hbar\omega - \frac{15\hbar^2 A^2}{2M^3\omega^4} \tag{2.12}$$

To find the Stark tuning rate, we must now consider the effect of applying an electric field $\vec{F}$. In the low field limit for a given set of nuclear coordinates $\vec{R}$ with associated dipole moment $\vec{\mu}(\vec{R})$, the total energy is shifted by $\vec{F}\cdot\vec{\mu}(\vec{R})$. The expansion of the vibrational potential (2.2) thus becomes:

$$\begin{aligned} V_F(\vec{R}) =& V(0) + \vec{F}\cdot\vec{\mu}(0) + \vec{F}\cdot\frac{\partial\vec{\mu}}{\partial R_i}R_i + \frac{1}{2}\frac{\partial^2 V}{\partial R_i \partial R_j}R_i R_j \\ &+ \frac{1}{2}\frac{\vec{F}\cdot\partial^2\vec{\mu}}{\partial R_i \partial R_j}R_i R_j + \frac{1}{6}\frac{\partial^3 V}{\partial R_i \partial R_j \partial R_k}R_i R_j R_k \end{aligned} \tag{2.13}$$

The dynamical matrix D is likewise perturbed by a term δD proportional to F. Assuming the vibrational mode of interest is non-degenerate, the perturbed mode $\tilde{q}$ subject to $(D+\delta D)\tilde{q}_i = \tilde{\lambda}_i\tilde{q}_i$ can be expressed in terms of the original modes:

$$\tilde{q}_i = \vec{q}_i + \sum_{j\neq i}\frac{\vec{q}_j^{\,T}\delta D\vec{q}_i}{\lambda_i - \lambda_j}\vec{q}_j = \vec{q}_i + \delta\vec{q}_i \tag{2.14}$$

Now the single dimensional potential becomes:

$$\begin{aligned} V_{qF}(x) = V_F(x\tilde{q}) =& V(0) + \frac{\partial V_F}{\partial R_i}(q+\delta q)_i x \\ &+ \frac{1}{2}\frac{\partial^2 V_F}{\partial R_i \partial R_j}(q+\delta q)_i (q+\delta q)_j x^2 \\ &+ \frac{1}{6}\frac{\partial^3 V_F}{\partial R_i \partial R_j \partial R_k}(q+\delta q)_i (q+\delta q)_j (q+\delta q)_k x^3 \end{aligned} \tag{2.15}$$

Expanding V_{qF} and keeping only those terms constant or linear in F leaves:

$$\begin{aligned} V_{qF}(x) =& V(0) + \vec{F}\cdot\vec{\mu}(0) + \vec{F}\cdot\frac{\partial\vec{\mu}}{\partial R_i}q_i x + \frac{\partial^2 V}{\partial R_i \partial R_j}\delta q_i q_j x^2 \\ &+ \frac{1}{2}\frac{\partial^2 V}{\partial R_i \partial R_j}q_i q_j x^2 + \frac{1}{2}\vec{F}\cdot\frac{\partial^2\vec{\mu}}{\partial R_i \partial R_j}q_i q_j x^2 \\ &+ \frac{1}{6}\frac{\partial^3 V}{\partial R_i \partial R_j \partial R_k}q_i q_j q_k x^3 + \frac{1}{2}\frac{\partial^3 V}{\partial R_i \partial R_j \partial R_k}\delta q_i q_j q_k x^3 \end{aligned} \tag{2.16}$$

Because δq and q are orthogonal and q is an eigenvector of the dynamical matrix, the term $\frac{\partial^2 V}{\partial R_i \partial R_j}\delta q_i q_j x^2$ disappears. The final term gives the impact of mode mixing. For diatomic molecules this term is identically zero, and was not significant for the other small molecules studied. Mapping the remaining terms into a perturbed harmonic oscillator Hamiltonian as before in (2.6), the vibrational Hamiltonian in the presence of an applied field becomes:

$$H_F(q) = \frac{p^2}{2M} + \frac{M\omega^2}{2}q^2 + Aq^3 + F\frac{\partial\mu}{\partial q}q + \frac{1}{2}F\frac{\partial^2\mu}{\partial q^2}q^2 \tag{2.17}$$

This can be recast in the form (2.6) with a constant shift of the coordinate

$q \to \tilde{q}$ and a new nominal frequency $\omega \to \tilde{\omega}$.

$$H_F(\tilde{q}) = \frac{p^2}{2M} + \frac{M\tilde{\omega}^2}{2}\tilde{q}^2 + A\tilde{q}^3 + const. \tag{2.18}$$

$$\tilde{\omega} = \sqrt{\frac{F}{M}\frac{\partial^2\mu}{\partial q^2} + \sqrt{\left(\omega^2 + \frac{F}{M}\frac{\partial^2\mu}{\partial q^2}\right)^2 - \frac{12A}{M^2}F\frac{\partial\mu}{\partial q}}} \tag{2.19}$$

As before the anharmonic corrections to the frequency yield $\nu_F = \hbar\tilde{\omega} - 15\hbar^2A^2/2M^3\tilde{\omega}^4$. The field dependent frequency shift can then be expressed as:

$$\nu_F - \nu = \hbar\left(\tilde{\omega}_F - \omega\right) - \frac{15A^2\hbar^2}{2M^3}\left(\tilde{\omega}_F^{-4} - \omega^{-4}\right) \tag{2.20}$$

Finally, the taking the first derivative of ν_F evaluated at $F = 0$ gives us the Stark tuning rate $\Delta\mu$.

$$\Delta\mu = \left.\frac{\partial\nu_F}{\partial F}\right|_{F=0} = \hbar\left.\frac{\partial\tilde{\omega}_F}{\partial F}\right|_{F=0} + \left.\frac{30\hbar^2A^2}{M^3\omega^5}\frac{\partial\tilde{\omega}_F}{\partial F}\right|_{F=0} \tag{2.21}$$

From (2.19) we find $\left.\frac{\partial\tilde{\omega}_F}{\partial F}\right|_{F=0}$ is given by $\frac{1}{M\omega}\frac{\partial^2\mu}{\partial q^2} - \frac{3A}{M^2\omega^3}\frac{\partial\mu}{\partial q}$. Substituting this into (2.21) and rearranging yields:

$$\Delta\mu = \left(\frac{\hbar}{2M\omega} + \frac{15\hbar^2}{M^4\omega^6}A^2\right)\frac{\partial^2\mu}{\partial q^2} - \left(\frac{3\hbar}{M^2\omega^3}A + \frac{90\hbar^2}{M^5\omega^8}A^3\right)\frac{\partial\mu}{\partial q} \tag{2.22}$$

Nonlinearity in the the dipole response $\mu(q)$ directly contributes to the Stark tuning rate, while the linear response $\frac{\partial\mu}{\partial q}$ only contributes through anharmonicities in the vibrational potential.

In practice the vibrational potential may possess more than a simple

cubic anharmonicity. Although algebraically tedious, higher order corrections to the vibrational potential shown in (2.23) can be accounted for with the same machinery of ladder operators and first and second order perturbation theory.

$$H(q) = \frac{p^2}{2M} + \frac{M\omega^2}{2}q^2 + Aq^3 + Bq^4 + Cq^5 \tag{2.23}$$

The contribution from Aq^3 is the same as before (2.10). The term Bq^4 gives both first and second order corrections:

$$\begin{aligned}
E_{n_B}^{(1)} &= \frac{\hbar^2 B}{4M^2\omega^2} \langle n| \left(a^\dagger + a\right)^4 |n\rangle \\
E_{n_B}^{(2)} &= \frac{\hbar^3 B^2}{16M^4\omega^5} \sum_{m\neq n} \frac{\left|\langle m| \left(a^\dagger + a\right)^4 |n\rangle\right|^2}{n-m} \\
E_{n_C}^{(1)} &= \left(\frac{\hbar}{2M\omega}\right)^{\frac{5}{2}} C \langle n| \left(a^\dagger + a\right)^5 |n\rangle = 0 \\
E_{n_C}^{(2)} &= \frac{\hbar^4 C^2}{16M^5\omega^6} \sum_{m\neq n} \frac{\left|\langle m| \left(a^\dagger + a\right)^5 |n\rangle\right|^2}{n-m}
\end{aligned} \tag{2.24}$$

Evaluating these expressions for $n = 0$ and $n = 1$ allows us to find the perturbed transition frequency $\nu = E_1 + E_1^{(1)} + E_1^{(2)} - E_0 - E_0^{(1)} + E_0^{(2)}$:

$$\nu = \omega + \frac{3\hbar B}{M^2\omega^2} - \frac{15\hbar A^2}{2M^3\omega^4} - \frac{18\hbar^2 B^2}{M^4\omega^5} - \frac{275\hbar^2 AC}{4M^4\omega^5} - \frac{665\hbar^3 C^2}{M^5\omega^6} \tag{2.25}$$

With this result, we can account for the electric field in the same manner

as (2.17):

$$H_F(q) = \frac{p^2}{2M} + \frac{M\omega^2}{2}q^2 + Aq^3 + Bq^4 + Cq^5 + F\frac{\partial\mu}{\partial q}q + \frac{1}{2}F\frac{\partial^2\mu}{\partial q^2}q^2 \qquad (2.26)$$

Shifting coordinates as in (2.18) and (2.19) to remove the linear term in the limit of small field strength F gives the field dependent transition frequency ν_F. To find the Stark tuning rate with up to fifth order anharmonic terms, we once again differentiate with respect to F:

$$\begin{aligned}\Delta\mu = \left.\frac{\partial\nu_F}{\partial F}\right|_{F=0} = \Bigg(&-\frac{3A\hbar}{M^2\omega^3} - \frac{15C\hbar^2}{M^3\omega^4} + \frac{78AB\hbar^2}{M^4\omega^6} + \frac{455BC\hbar^3}{M^5\omega^7} - \frac{90A^3\hbar^2}{M^5\omega^8} \\ &- \frac{4125A^2C\hbar^3}{4M^6\omega^9} - \frac{270AB^2\hbar^3}{M^6\omega^9} - \frac{5985AC^2\hbar^4}{2M^7\omega^{10}}\Bigg)\frac{\partial\mu}{\partial q} \\ &+ \Bigg(\frac{\hbar}{2M\omega} - \frac{3B\hbar^2}{M^3\omega^4} + \frac{15A^2\hbar^2}{M^4\omega^6} + \frac{1375AC\hbar^3}{8M^5\omega^7} \\ &+ \frac{45B^2\hbar^3}{M^5\omega^7} + \frac{1995C^2\hbar^4}{4M^6\omega^8}\Bigg)\frac{\partial^2\mu}{\partial q^2}\end{aligned} \qquad (2.27)$$

2.1.2 Computational Details

Calculating the tuning rate from (2.22) or (2.27) requires determination of the shape of the potential energy surface and the dipole moment as a function of displacement $\mu(q)$. For the two diatomic species CO and CN^-, this information is obtained by simply by repeatedly performing a DFT total energy calculating while varying the internuclear distance. The CO internuclear distance was varied from 1.75 to 2.55 a_0 over 17 steps. The grid spacing was 0.2 a_0, and pseudopotentials were generated with the cutoff radii given in

Table 2.1.

Table 2.1: Pseudopotential data

Atom	Configuration	s-cutoff (a_0)	p-cutoff (a_0)	Local component
H	$1s^2$	1.49	-	s
C	[He]$2s^2$ $2p^2$	1.49	1.52	p
N	[He]$2s^2$ $2p^3$	1.50	1.50	p
O	[He]$2s^2$ $2p^4$	1.48	1.48	p

The total energy as a function of bond length was fit to a polynomial of third or fifth order to determine the parameters ω and A of (2.6) or ω, A, B, and C of (2.23) (the constant term is ignored as it does not affect solutions to the Hamiltonian). A sample set of data points and resulting fit are seen in Figure 2.1. The dipole moment function $\mu(q)$ is determined similarly. While Section 1.1 focused on the development of DFT for solving the total energy and electronic structure, extracting the dipole moment from these results is straightforward since the total charge density is solved for as part of that process. The resulting dipole moment can then be found by:

$$\vec{\mu} = -\int n(\mathbf{r})\mathbf{r}d^3\mathbf{r} + \sum_{i=1}^{N_{at}} Z_i\mathbf{R_i} \tag{2.28}$$

where $n(\mathbf{r})$ is the charge density, Z_i is the nuclear charge of the i^{th} atom, and N_{at} is the total number of atoms. The corresponding data can be seen in Figure 2.2. The first and second derivatives $\partial\mu/\partial q$ and $\partial^2\mu/\partial q^2$ are easily obtained from the corresponding fit.

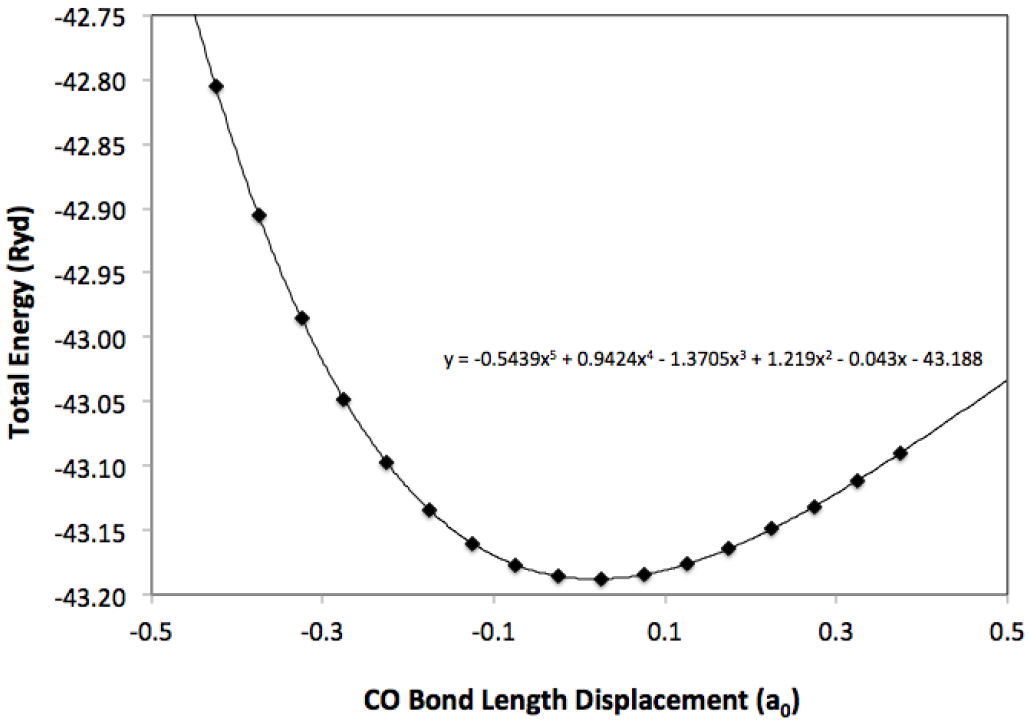

Figure 2.1: Variation of the DFT calculated total energy for CO as a function of bond length displacement. A fifth order polynomial fit is included.

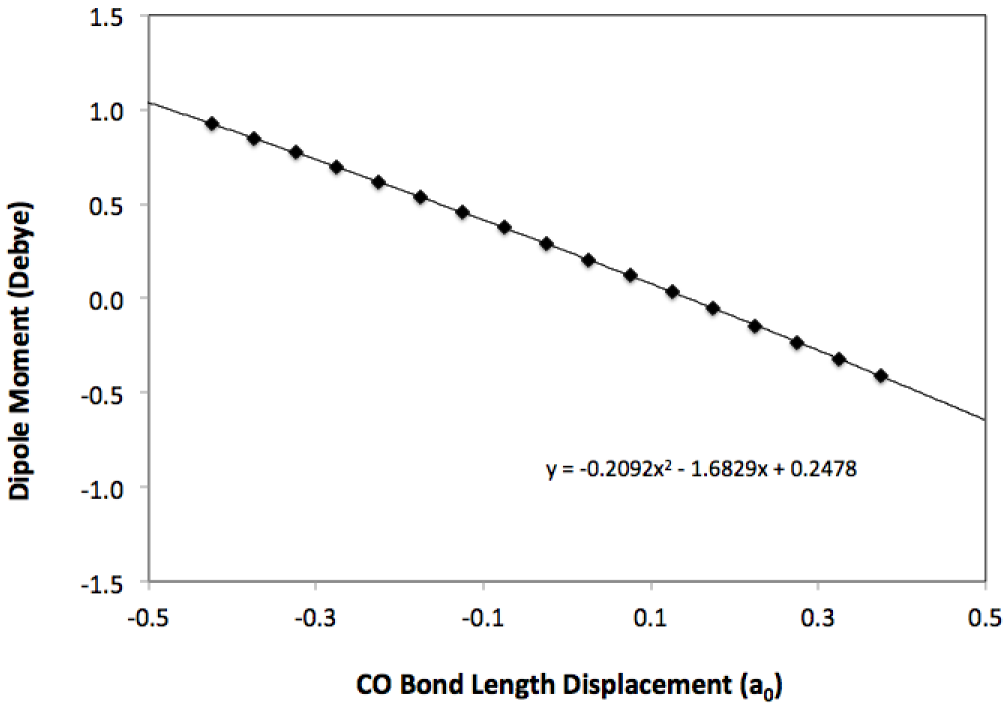

Figure 2.2: The dipole moment of CO as a function of bond length displacement. A second order polynomial fit is included.

2.1.3 Results

We evaluate the cubic and quintic perturbative expressions (2.12) and (2.25). The resulting values are compared with experimental results in Table 2.2.

Table 2.2: Perturbative approximations to the vibrational frequency versus experimental values.

Molecule	Cubic Pert	Quintic Pert	Expt.
CO	2127	2078	2143
CN^-	2063	2043	2080
Acetone	1786	1705	1711
BCN	2382	2234	2228

Naively, one might expect the harmonic approximation to be accurate enough to calculate the vibrational frequency – in the limit of vanishing displacements from equilibrium position, the potential energy surface should approach a quadratic form. However, infinitesimal displacements are only possible in a classical treatment of vibration. As illustrated in Figure 2.3, the ground state energy sets a minimum length scale for the domain of the vibrational potential. The fundamental transition frequency requires we consider also the first excited mode. As seen in Figure 2.3, anharmonic contributions to the shape of the potential for CO are visible to the naked eye as early as the first excited mode. This is reflected in the results of Table 2.2 – a harmonic potential with cubic perturbations is sufficient to calculate the frequency within approximately 5%. However, including quintic perturbations to more accurately reflect the shape of the potential dramatically reduces the errors of the polyatomic species down to less than 0.5%. The accuracy of the polyatomic

species also indicates that the dynamical matrix (2.3) and associated displacement vectors (2.4) are well resolved. As the dynamical matrix is calculated from Hellmann-Feynman forces, it is more sensitive to convergence than the total energy calculations that make up the potential energy surface.

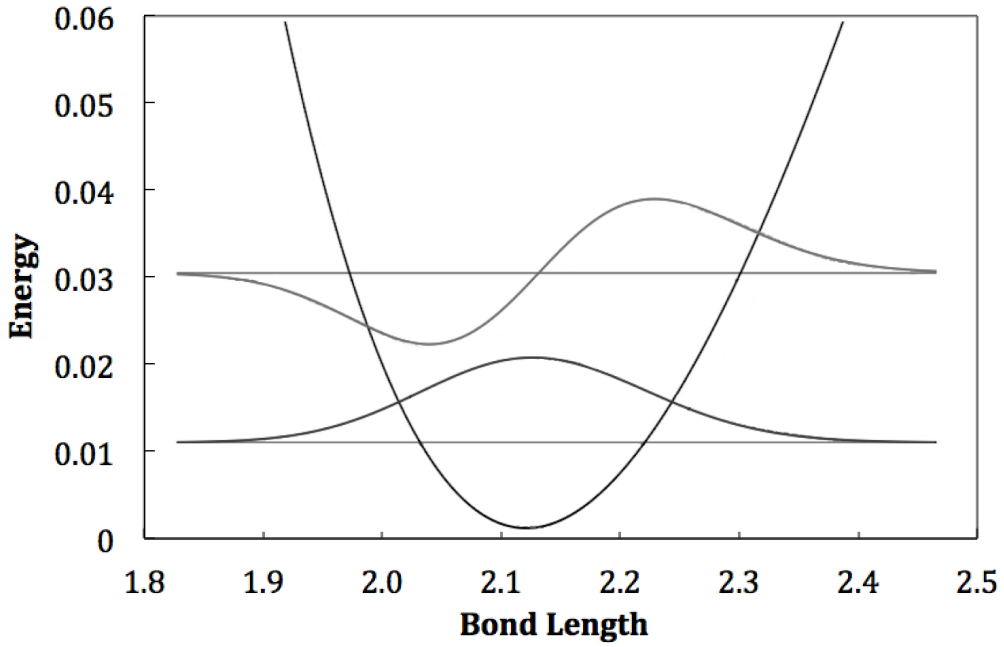

Figure 2.3: Ground state and first excited vibrational modes for the CO molecule overlaid on the potential energy surface. Horizontal lines show the energy for each mode relative to the classical minimum.

Table 2.3 lists the calculated perturbative results with cubic and quintic potentials as compared to experimental results. The diatomic species CO and CN^- are seen to be in good agreement with literature values. The polyatomic species, however, yield tuning rates significantly smaller than the literature suggests.

To see if there are clues about the discrepancy between the tuning rate accuracy for large and small molecules, Tables 2.4 and 2.5 list the contribu-

Table 2.3: Perturbative approximations to the Stark tuning rate versus experimental values.

Molecule	Cubic Pert	Quintic Pert	Expt.[a]
CO	0.50	0.44	0.43 – 0.67
CN^-	0.20	0.22	0.22[b]
Acetone	0.52	0.52	0.75
BCN	0.28	0.28	0.61

[a]References [34] and [30], all values in $cm^{-1}/(MV/cm)$.
[b]Experimental values not known for ion, calculated value from [31]

tions of the individual terms to the tuning rate. The direct nonlinear dipole response term $\frac{\hbar}{2M\omega}\frac{\partial^2\mu}{\partial q^2}$ contributes notably in acetone; however, in all cases the largest contribution comes from coupling between the cubic anharmonicity in the potential A and the linear response of the dipole $\partial\mu/\partial q$. If $\partial\mu/\partial q$ is thought of as giving rise to a shift in the equilibrium position as a function of applied electric field, then this term comes from the shifting curvature of the potential at that minimum. This suggests the tuning rate is sensitive to geometric distortion, and the larger species may then be more sensitive to the environmental factors implicit in experimental measurements. In the next section we employ a more direct finite field method to better account for the experimental results.

Table 2.4: Component contributions to the cubic model of the tuning rate.

Term	CO	CN^-	Acetone	BCN
$-\frac{3\hbar A}{M^2\omega^3}\frac{\partial\mu}{\partial q}$	0.4262	0.1930	0.6749	0.1519
$-\frac{90\hbar^2A^3}{M^5\omega^8}\frac{\partial\mu}{\partial q}$	0.0398	0.0113	0.0451	0.0065
$\frac{\hbar}{2M\omega}\frac{\partial^2\mu}{\partial q^2}$	0.0283	-0.0056	-0.1893	0.0807
$\frac{15\hbar^2A^2}{M^4\omega^6}\frac{\partial^2\mu}{\partial q^2}$	0.0026	-0.0003	-0.0126	0.0035

Table 2.5: Component contributions to the quintic model of the tuning rate.

Term	CO
$-\frac{3\hbar A}{M^2\omega^3}\frac{\partial\mu}{\partial q}$	0.4047
$-\frac{15\hbar^2 C}{M^3\omega^4}\frac{\partial\mu}{\partial q}$	0.0071
$\frac{78\hbar^2 AB}{M^4\omega^6}\frac{\partial\mu}{\partial q}$	-0.0343
$\frac{455\hbar^3 BC}{M^5\omega^7}\frac{\partial\mu}{\partial q}$	-0.0007
$-\frac{90\hbar^2 A^3}{M^5\omega^8}\frac{\partial\mu}{\partial q}$	0.0328
$-\frac{4125\hbar^3 A^2 C}{4M^6\omega^9}\frac{\partial\mu}{\partial q}$	0.0013
$-\frac{270\hbar^3 AB^2}{M^6\omega^9}\frac{\partial\mu}{\partial q}$	0.0004
$-\frac{5985\hbar^4 AC^2}{2M^7\omega^{10}}\frac{\partial\mu}{\partial q}$	1.33×10^{-5}
$\frac{\hbar}{2M\omega}\frac{\partial^2\mu}{\partial q^2}$	0.0294
$-\frac{3\hbar^2 B}{M^3\omega^4}\frac{\partial^2\mu}{\partial q^2}$	-0.0006
$\frac{15\hbar^2 A^2}{M^4\omega^6}\frac{\partial^2\mu}{\partial q^2}$	0.0024
$\frac{1375\hbar^3 AC}{8M^5\omega^7}\frac{\partial^2\mu}{\partial q^2}$	9.51×10^{-5}
$\frac{45\hbar^3 B^2}{M^5\omega^7}\frac{\partial^2\mu}{\partial q^2}$	2.80×10^{-5}
$\frac{1995\hbar^4 C^2}{4M^6\omega^8}\frac{\partial^2\mu}{\partial q^2}$	9.62×10^{-7}

2.2 Finite Field Method

While the perturbative methods explored in the last section are expected to accurately account for the effects of the electric field on the total energy, there is greater uncertainty in the process of translating that effect into vibrational frequencies and tuning rates. One advantage of working with non-periodic cluster boundary conditions is our ability to impose arbitrary finite fields with little complication.

2.2.1 Computational Details

To tackle this problem, we make use of real-space density functional theory wherein the Kohn-Sham equation is solved self consistently on a uniform cubic grid in real space. Without neighboring dipole interactions, large supercells can be avoided. [35, 36] Charged systems such as CN^- are easily handled without compensating background charges. With a finite spatial domain, finite electric fields can be applied with a simple modification of the Kohn-Sham equation:

$$\left[-\frac{\hbar^2\nabla^2}{2m} + V_{\text{eff}}(\vec{r}) - e\vec{F}\cdot\vec{r}\right]\psi_n(\vec{r}) = E_n\psi_n(\vec{r}) \tag{2.29}$$

where $V_{\text{eff}}(\vec{r})$ includes the ionic pseudopotentials, Hartree potential, and exchange-correlation potential. The applied field is $\vec{F}$. This finite field real space method has previously been demonstrated to accurately account for the polarizabilities of small molecules and clusters with fixed geometry. [37, 38]

Given the numerical sensitivity of this problem, convergence is critical. The cubic grid that the wave functions are defined on is controlled by a single parameter – the grid spacing h. Convergence can be checked by reducing the size of h. This is considerably simpler than explicit basis methods where the basis functions required for convergence may change with varying geometries and polarizing fields.

DFT calculations were performed using PARSEC. [4] The wave functions are calculated self-consistently on a cubic Cartesian grid. The grid spacing h had typical values ranging from 0.15 to 0.30 bohr. Cluster boundary conditions are implemented by requiring the wave functions to vanish at the

edges of a domain. For small molecules, we typically use a bounding sphere with radius 7 to 8 bohr larger than the half-width of the molecule. This ensures that the wave functions are vanishingly small where they meet the boundary. The appropriateness of the bounding sphere can be confirmed by verifying the total energy and force calculations are conserved with respect to increases in the bounding radius.

Troullier-Martins [9] pseudopotentials are employed with the p orbitals taken to be the local component since the s component yields a simpler projection operator. Cutoff radii are given in Table 2.1. Exchange-correlation was handled with the Ceperley-Alder LDA functional. [7]

Table 2.6: Pseudopotential data

Atom	Configuration	s-cutoff (a_0)	p-cutoff (a_0)	Local component
H	$1s^2$	1.49	-	s
C	[He]$2s^2$ $2p^2$	1.49	1.52	p
N	[He]$2s^2$ $2p^3$	1.50	1.50	p
O	[He]$2s^2$ $2p^4$	1.48	1.48	p

To find a particular stretching mode, we begin by constructing the dynamical matrix:

$$D_{Ii,Jj} = \frac{1}{\sqrt{M_I M_J}} \frac{\partial F_{Ii}}{\partial R_{Jj}} \tag{2.30}$$

where the indices I and J run across all atoms, and the indices i and j run across the x, y, and z axes. F_{Ii} is the force on the Ith atom in the i direction, and R_{Jj} is the jth cartesian coordinate of the Jth atom. Atomic forces are calculated by the Hellmann-Feynman theorem in PARSEC. As proposed by Parlinski et al. [39] the partial derivative with respect to R_{Jj} is calculated

with finite differencing. With a positive and negative displacement along each axis for N atoms, this requires $6N + 1$ total converged DFT calculations to determine the dynamical matrix.

Once the dynamical matrix is found, the vibrational modes can be found by diagonalizing the matrix. While the vibrational frequencies can be taken directly from the matrix eigenvalues, these frequencies lack any anharmonic corrections. Instead, we take the selected eigenmode $\vec{u}$ which is expressed in mass weighted coordinates and use it to find the atomic displacements $\vec{q}$ for the pertinent stretching mode.

$$q_{Ii}^{n} = \frac{1}{\sqrt{M_I}} u_{Ii}^{n} \tag{2.31}$$

This allows us to find the one-dimensional vibrational potential $U(x)$ as a function of the total electronic energy of the system for finite displacements along the mode $E(\vec{R}_{eq} + x\vec{q})$. As $U(x)$ is a one dimensional slice of the full potential energy surface $E(\vec{R})$, it picks up the anharmonic components relevant to that mode. To explicitly find the anharmonic vibrational energy levels we construct the 1D Schrodinger equation for this system.

$$-\frac{\partial^2 \psi_n}{\partial x^2} + U(x)\psi_n = \mathcal{E}_n \psi_n \tag{2.32}$$

The bound states of this system are readily found by numerical integration. We implement the Numerov-Cooley method [40, 41] which iteratively finds the energies and eigenfunctions. The reported frequency is then given by the fundamental transition from the ground state to the first excited vibra-

tional state $(\mathcal{E}_1 - \mathcal{E}_0)/hc$.

To determine the dependence on the electric field, a new vibrational potential $U_F(x)$ is found by repeating the DFT total energy calculations in the presence of a finite field for the coordinates $E_F(\vec{R}_{eq} + x\vec{q})$. Again, the vibrational energy levels of this new potential are found via the Numerov-Cooley method, and the frequency as a function of field strength is generated, as seen in Figure 1. Figure 2 illustrates the perturbation of the energy surface and associated vibrational states with an enhanced field to exaggerate the differences. The tuning rate $\Delta\mu$ is then found by fitting the frequency $\tilde{\nu}(F)$ to the quadratic expression $\tilde{\nu}_0 + \Delta\mu F + \frac{1}{2}\alpha F^2$.

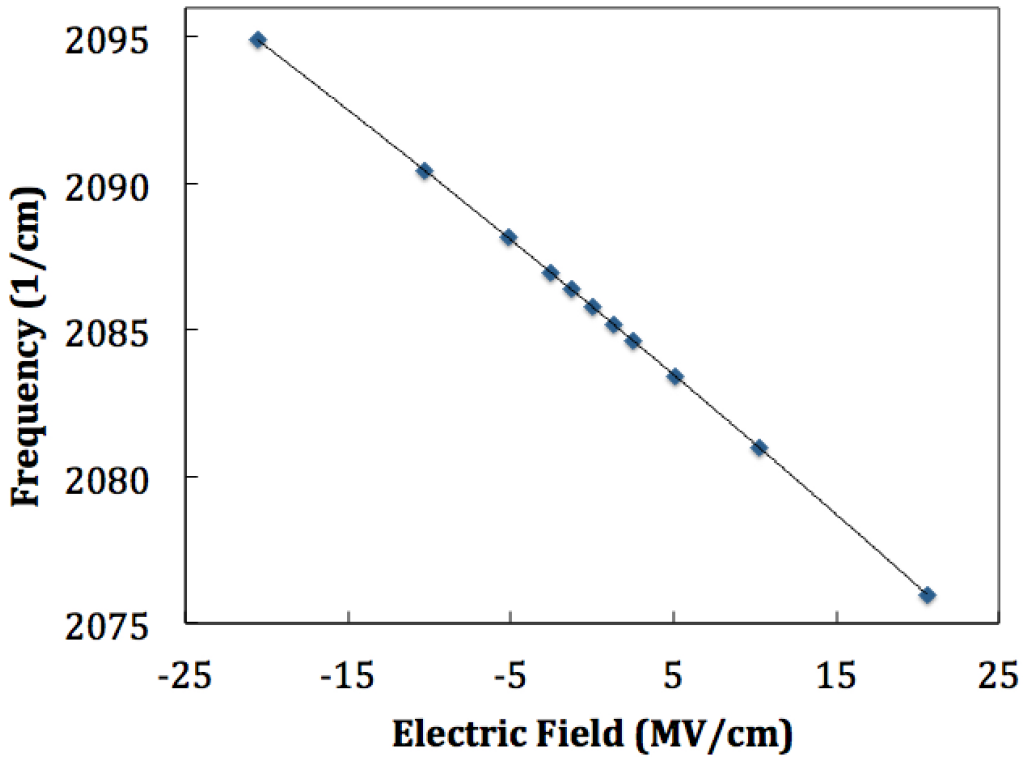

Figure 2.4: Variation of vibrational frequency as a function of applied field.

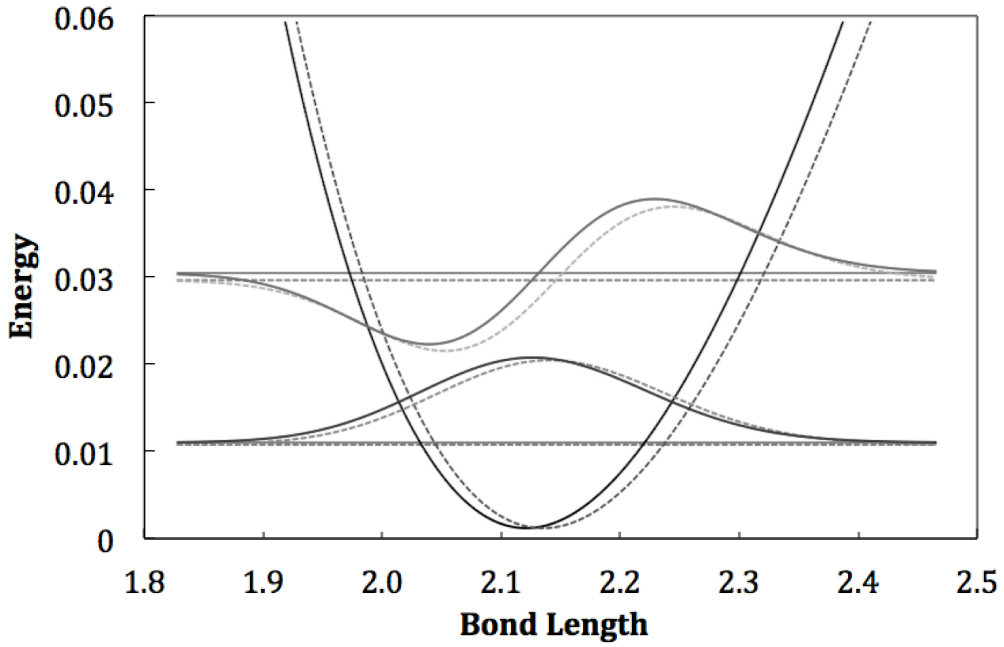

Figure 2.5: Original (solid) and perturbed (dashed) potential energy surface under a large field, along with first and second vibrational modes. Horizontal lines show the energies for given modes.

2.2.2 Results

The results of the finite field method are summarized in Table 2.7 and compared with experimental values.

Table 2.7: Finite field method results for the frequency and Stark tuning rate versus experimental values

Molecule	MD ν	Expt. ν	MD $\Delta\mu$	Expt. $\Delta\mu$
CO	2085	2143	0.46	0.43 – 0.67
CN^-	2044	2080	0.22	...
Acetone	1708	1711	0.51	0.75
BCN	2238	2228	0.33	0.61

We observe good agreement with vibrational frequencies, and tuning rates for the diatomic molecules in agreement other work.

2.2.3 Higher Order Methods for Interatomic Forces

While the methods of the previous section are primarily dependent on DFT total energy calculations, force calculations are critical to setting up the problem – finding the ground state structure and calculating the dynamical matrix. To avoid using finite differencing on the total energy, which would require multiple converged DFT calculations for every nuclear force component, Hellmann-Feynman forces are instead used. Calculating the Hellmann-Feynman forces involves derivates of the ionic potential, which change significantly over the length scale of typical grid spacings. This means that the force calculations are generally more sensitive and slower to converge as a function of grid spacing.

The Hellmann-Feynman theorem states that:

$$\frac{dE}{d\lambda} = \int \psi^* \frac{d\hat{H}}{d\lambda} \psi dV \tag{2.33}$$

where E is the total energy for the system with Hamiltonian $\hat{H}$, and λ is any chosen parameter of $\hat{H}$. Therefore, to calculate the force on the i^{th} atom, we need to evaluate an expression of the form:

$$\mathbf{F}_i = -\sum_{j}^{N_{occ}} \langle \phi_j | \nabla_i \hat{H}(\mathbf{R}_i) | \phi_j \rangle \tag{2.34}$$

Critically, of the terms in the Hamiltonian, only the ionic potential with its explicit dependence on $\mathbf{R}_i$ factors into determining the forces.

Conventionally the spatial integration in (2.34) is carried out by a simple Riemann sum in PARSEC. As described in [42], a variation of PARSEC

was developed that instead used a Gaussian quadrature to compute these integrals and take advantage of the fact that the ionic potential is known with greater detail than the grid points can describe (as the pseudopotentials are calculated independently). As demonstrated elsewhere [42], this higher order (HO) method allows the forces to converge at significantly larger grid spacings, representing important savings in computational resources needed, as well as smoothing out numerical errors that can arise as the distance between nuclei and grid points changes.

Given the sensitivity of the Stark tuning rate to convergence and numerical noise, we tested the finite field method in this HO version of PARSEC. Figure 2.6 compares results for both the frequency and tuning rate with the newer HO method as well as the prior version of the code (LO) as a function of grid spacing. Our results replicate the significant improvement in convergence reported in previous work [42].

The LO and HO methods converge at grid spacings of approximately 0.15 a_0. Promisingly, the HO method conserved both the vibrational frequency and the tuning rate to within 1% at grid spacings up to 0.25 a_0. This represents a reduction in the number of grid points needed by a factor of 4.6.

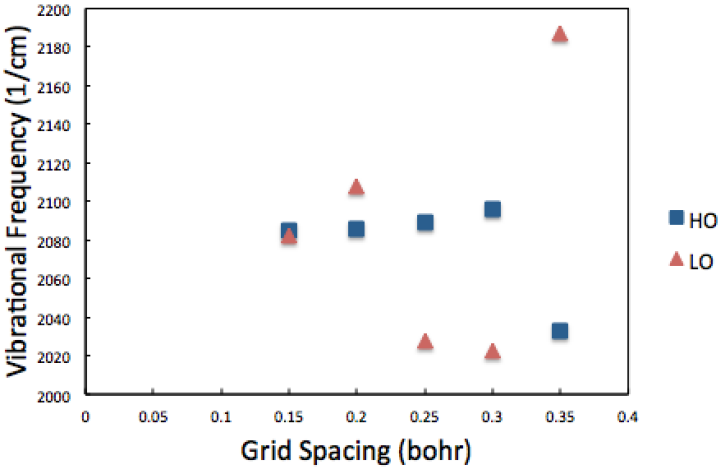

(a)

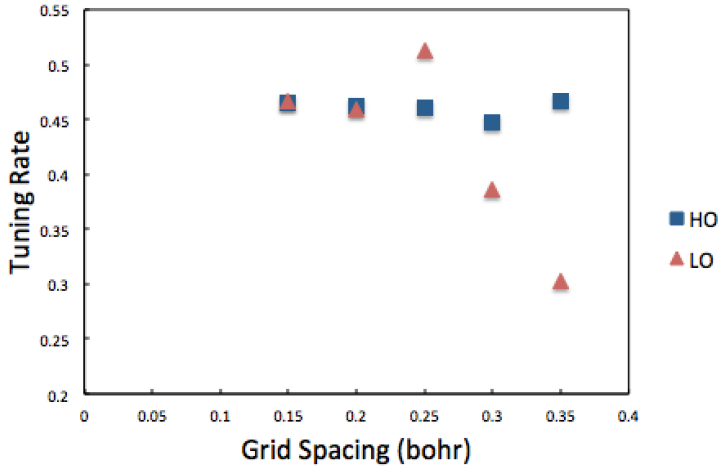

(b)

Figure 2.6: Convergence of the CO (a) vibrational frequency and (b) tuning rate with HO and LO methods.

2.3 Molecular Dynamics

Both the perturbative and finite field methods discussed in the prior two sections rely on the use of the dynamical matrix to explicitly focus on the desired vibrational mode. However, as evidenced by the results of the perturbative analysis, the Stark tuning rate primarily arises due to the interactions between vibrational anharmonicity and the dipole response of the molecule. Further, as seen in Figure 2.3, the harmonic approximation begins to break down even in the lowest energy vibrational states. This raises the question of whether it is appropriate to start our calculations from the implicitly harmonic basis of the dynamical matrix.

2.3.1 Computational Details

While the perturbative method outlined above provides a check on the finite field method, it still explicitly depends on the vibrational modes determined by the dynamical matrix. As an alternative, vibrational frequencies can

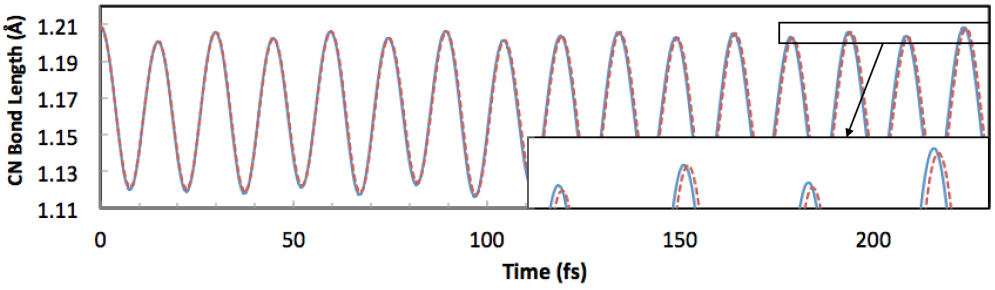

Figure 2.7: Change in the CN bond length of benzonitrile as a function of time with (dashed line) and without (solid line) an applied field of 7.71 MV/cm. Inset shows the slowly growing divergence between the simulations.

also be calculated using *ab initio* molecular dynamics (MD). This is an attractive option because at no stage must we assume the vibrations are harmonic nor that the structure is fully relaxed. Unlike many traditional molecular dynamics approaches which make use of classical and empirical interatomic potentials to calculate the forces acting on atoms, *ab initio* molecular dynamics performs a fully quantum mechanical DFT calculation at every time step. As in previous real space MD work [13,36,43], the Born-Oppenheimer approximation is assumed, the Kohn-Sham equation is solved self consistently at each time step, and atomic forces are calculated by the Hellmann-Feynman theorem. Nuclear coordinates are updated using Beeman's algorithm [44]. The update nuclear coordinates are given by:

$$\mathbf{R}_i(t+\Delta t) = \mathbf{R}_i(t) + \mathbf{v}_i(t)\Delta t + \frac{1}{6}\left(4\mathbf{a}_i(t) - \mathbf{a}_i(t-\Delta t)\right)\Delta t^2 \tag{2.35}$$

where $\mathbf{R}_i(t)$ is the i^{th} nuclear coordinate at time t, $\mathbf{v}_i$ is the velocity of the i^{th} nucleus, and $\mathbf{a}_i$ is the acceleration of the nucleus, given by the Hellmann-Feynman force divided by the appropriate nuclear mass.

To excite the relevant modes, the pertinent bond length was perturbed by stretching along the bond axis by approximately 0.1 Å and then the system was allowed to evolve in time. Time steps as small as 0.2 fs were used to ensure accuracy and a thorough sampling of the potential energy surface. The simulation was allowed to run for 1200 time steps. The frequency was recovered from the simulation by taking the power spectrum of the pertinent bond length

as a function of time and plotting the intensity:

$$P(\omega) = \frac{1}{T}\int_0^T d(t)e^{-i\omega t}dt \tag{2.36}$$

To find the tuning rate, the MD simulation was simply repeated in the presence of a finite field in the same form as before. Field strengths used were 0, 2.57, and 7.71 MV/cm (or 0, 1×10^{-3}, and 3×10^{-3} Ryd/a_0). The tuning rate was calculated for different simulation lengths to ensure convergence. The perturbing effect of the field on the nitrile bond length of benzonitrile is illustrated in Figure 3.

The energy drift for this system is shown, along with the potential energy fluctuations, in Figure 4. The system is not coupled to a heat reservoir, nor is conservation of energy explicitly enforced. Small errors in the forces and numerical error from finite time steps lead to stochastic noise in the total energy, which is seen to drift by less than 5 meV/ps per atom. Given that room temperature thermal fluctuations are of the order 20 meV, this drift is not considered significant.

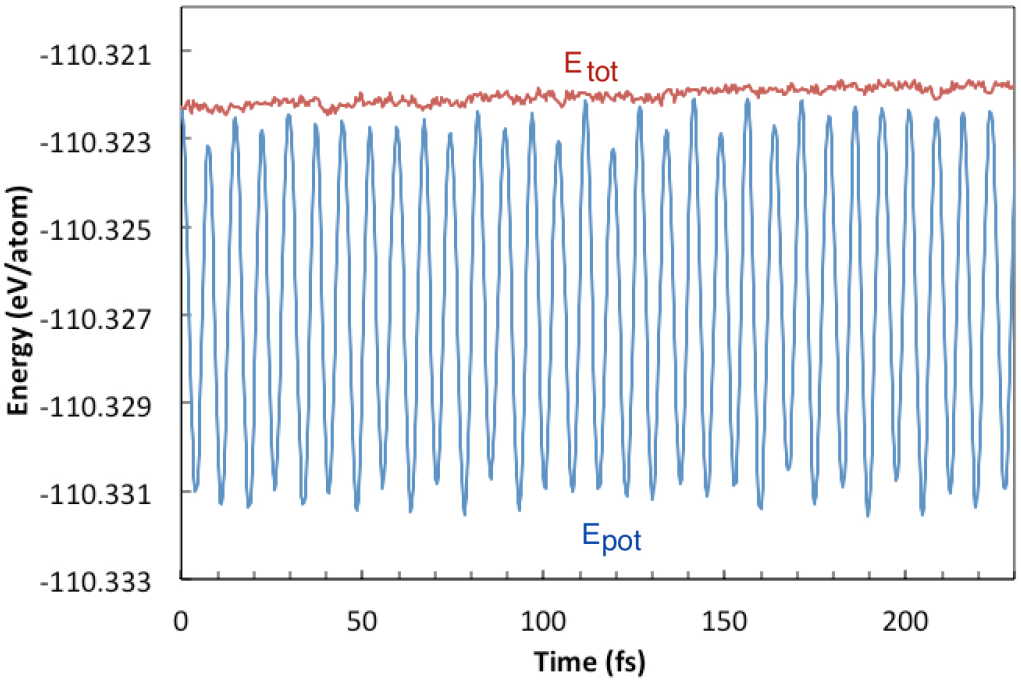

Figure 2.8: Variation of potential and total energy as a function of time for benzonitrile.

2.3.2 Results

The results of the molecular dynamics method are summarized in Table 2.8 and compared with experimental values.

The net charge of the cyanide ion CN^- causes the molecule to experience a net force under applied fields. During the course of an MD simulation, this net force would cause the molecule to drift out of the domain of the simulation. For this reason CN^- is omitted from Table 2.8.

Table 2.8: Molecular dynamics results for the frequency and Stark tuning rate versus experimental values.

Molecule	MD ν	Expt. ν	MD $\Delta\mu$	Expt. $\Delta\mu$
CO	2066	2143	0.52	0.43 – 0.67
Acetone	1681	1711	0.52	0.75
BCN	2238	2228	0.34	0.61

2.4 Discussion

Table 2.9 provides a comparison of the calculated tuning rates across all three methods.

Table 2.9: Comparison of finite field, perturbative, and MD calculations of the tuning rate. Units are in $cm^{-1}/(MV/cm)$.

Molecule	$\Delta\mu$ FF	$\Delta\mu$ cubic pert	$\Delta\mu$ quintic pert	$\Delta\mu$ MD
CO	0.46	0.50	0.44	0.52
CN^-	0.22	0.20	0.22	-
Acetone	0.51	0.52	0.52	0.52
Benzonitrile	0.33	0.28	0.28	0.34

We have demonstrated that real space methods provide a computationally efficient and theoretically straightforward method for the calculation of vibrational Stark effect. The agreement between the direct finite field method and the perturbative approach verifies our single-dimensional model that illustrates how the dipole moment interacts with anharmonicities in the vibrational mode to give rise to the Stark tuning rate. The MD method is independent of the dynamical matrix and its assumption of harmonic vibrations. The agreement between the MD and direct approaches shows that they both capture the pertinent anharmonic behavior. The agreement between all three methods demonstrates the robustness of our solution for this numerically sensitive

calculation.

The larger question of why calculations underestimate experimental results remains. To understand this, we must understand the differences between our computational models and the experimental set ups. Judging the computational results purely by their agreement to experiment is dangerous – for example, Dalosto *et al.* [1] provide the calculated tuning rates as a function of basis set and applied field direction. Their results are reproduced in Table 2.10. They find a very strong dependence on the basis set used. Similarly, in Figure 2.6, the reported tuning rate can be found to range significantly above and below the converged value as a function of grid spacing.

Table 2.10: Effect of basis set on calculated Stark tuning rate for 4-chlorobenzonitrile as calculated by Dalosto *et al.* [1]

Basis set	$\Delta\mu_-$	$\langle\Delta\mu\rangle$	$\Delta\mu_+$
6-31G	0.371	0.465	0.56
6-31G(d)	0.292	0.394	0.497
6-31G(d,p)	0.294	0.395	0.496
6-31+G(d)	0.397	0.513	0.630
6-31++G	0.37	0.58	0.62
6-31++G(d)	0.38	0.51	0.64
6-311G(d)	0.30	0.435	0.57
6-311G(d,p)	0.30	0.435	0.57
6-311G(2d,2p)	0.42	0.504	0.59

To understand the discrepancy between experiment and calculation, we must consider the practical differences between experimental and computational set ups. The computational settings are fairly straightforward – an isolated molecule in vacuum is exposed to an electric field. The experimental world is much more complicated. Generally, experiments take place with the target molecule dissolved in a solvent or adsorbed to a surface [34]. The field

experienced by the probe is then not simply that the bare vacuum, but dependent on the complex local environment. Multiple sources [1, 31, 45] reference local field corrections in the range of 1.1 to 1.4. At the high end, a 40% correction would certainly bring our results more in line with experiment. However, there is another factor to consider – as seen in our perturbative analysis, one of the primary contributors to the Stark tuning rate is the effect of the electric field on the equilibrium bond length. These very small geometry shifts may be dwarfed by the effect of solvation. Results from Raman spectroscopy on CN and CO bonds show the composition of the solvent can change frequency peaks by tens of inverse centimeters [46]. It should come as little surprise then that geometry and corresponding potential energy surfaces of our vacuum scenarios do not exactly match those of the experimental scenarios.

Calculating the traditional dynamical matrix is less straightforward for a molecule dissolved in a solvent. However, in a few years it may be routine to run *ab initio* molecular dynamics simulations in such an environment. Our work demonstrates it may be feasible to recover the tuning rate from such simulations for a fully *ab initio* account of the vibrational Stark effect.

Chapter 3

2D Materials Under Applied Fields

Interest in molecularly thin two-dimensional (2D) materials has dramatically grown with the isolation and study of graphene. While graphene has remarkable properties, it is not a semiconductor, and recent attention has diverted to looking at a broader class of 2D materials that could have the mechanical and electronic properties necessary for novel electronic devices. Notably, while graphene has no band gap, many new 2D materials are semiconductors whose band gap and structure varies significantly from their bulk counterparts. Molybdenum disulfide, one of the most prominent members of the class of transition metal dichalcogenides, is already being studied both experimentally and computationally for its potential use in field effect transistors. [47–49]

The ability of real-space methods to handle mixed boundary conditions in a straightforward and efficient manner makes it very useful in the search for functional properties in this new class of materials. In traditional plane-wave DFT methods, mixed boundary conditions can be handled by retaining the 3D periodic structure and introducing a large vacuum region along non-periodic axes. When examining 2D materials that are under applied fields or may be polarized, long range interactions between sheets in different supercells are significant. As Yu, Stewart, and Tiwari write [50]:

> However, repeated calculations with varying unit-cell sizes have

shown that for systems such as films and nanowires, these dielectric constant values strongly depend on supercell size, an issue which has been brought up in other literature. Since the present calculations are performed using a periodic unit cell, the calculated dielectric constant is not for an isolated stack of graphene but rather a multilayer system consisting of graphene stacks separated by 30 bohr vacuum regions.

3.1 Polarizabilities of 2D Materials

The application of electric fields to 2D materials is complicated by the polarization of the field in response. The bare field applied in Equation 1.25 is screened by the electrons of the material. This response of the charge distribution is determined by the material's polarizability. In the general case this takes the form:

$$\mathbf{p}_i = \sum_j \alpha_{ij} \mathbf{F}_j \tag{3.1}$$

where $\mathbf{p}_i$ is the local induced dipole in direction i, $\mathbf{F}_j$ is the local electric field component in direction j, and α_{ij} is the polarizability tensor. For a 2D material and transverse field, this reduces to:

$$\mathbf{m} = \alpha \mathbf{F}_\perp / S \tag{3.2}$$

where $\mathbf{m}$ is the dipole per unit area and S is the surface area per unit cell. [50, 51] This polarizability can also be related to the materials dielectric constant

ϵ by the slab Clausius-Mossotti formula:

$$\alpha = \frac{\Omega}{4\pi}\frac{\epsilon - 1}{\epsilon} \tag{3.3}$$

with Ω representing the volume of a cell containing the material and ϵ is the dielectric constant for that particular region Ω. As the number of layers increases, this can then be compared to the bulk properties with the modified formula:

$$\alpha(N) = N\frac{\Omega_B}{8\pi}\frac{\epsilon_B - 1}{\epsilon_B} + 2\alpha_S \tag{3.4}$$

where N is the number of layers, Ω_B is the volume of the unit cell for the bulk structure, ϵ_B is the bulk dielectric constant, and α_S allows for the slight change in polarizable volume between surface and interior layers.

This framework gives us a quick method to test the efficiency of real space methods for 2D materials. As before, we apply a field to the test material by modifying the local potential of the Kohn-Sham equations. However within a material, electrons will move in response to the electric field, screening the applied field such that measured fields will be smaller. The contribution of the electrons to the electric potential is already captured by the Hartree potential V_H. This means we can recover the screened field via:

$$F = -\frac{\partial}{\partial z}\langle \Delta V_{ion} + \Delta V_H \rangle_{xy} \tag{3.5}$$

where ΔV_{ion} and ΔV_H are the differences between the local and Hartree potentials in the presence or absence of the applied field. This value is averaged over the periodic axes of the unit cell. Figure 3.1 illustrates how $\langle \Delta V_{ion} + \Delta V_H \rangle_{xy}$

varies as a function of the z axis in a multilayer system.

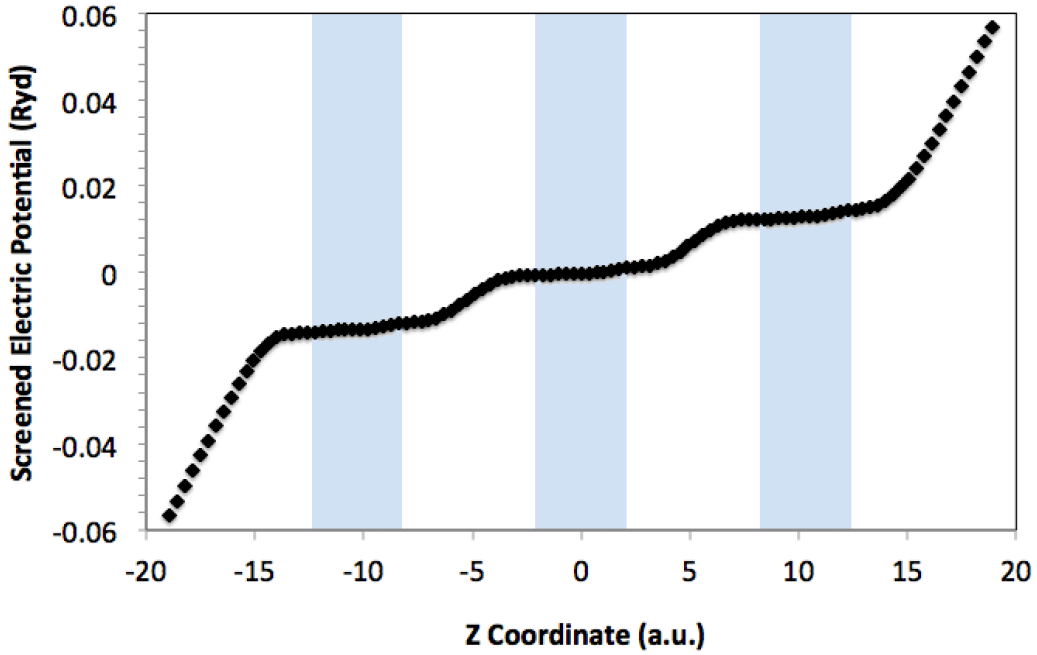

Figure 3.1: The screened electric potential of trilayer phosphorene subjected to a field of 25.7 MV/cm. The screened potential is recovered as $\langle \Delta V_{ion} + \Delta V_H \rangle_{xy}$. The shaded areas indicate the spans covered by the nuclei of each phosphorene layer.

3.2 Tuning Band Structures via Electric Fields

3.2.1 Opening a Gap in Graphene

While graphene is the most studied 2D material, owing to its many exciting properties, its unique band structure has no gap, limiting its application to semiconductor devices. Doping is one possible avenue to alter the band structure and introduce a gap, but comes with its own challenges. Experimental work demonstrated the carrier concentrations and mobilities could

be altered by a gate voltage [52]. Theoretical work utilizing a tight binding model has shown that a small gap could also be introduced by the presence of a transverse field in bilayer graphene [53,54]. Min *et al.* replicated this finding with *ab initio* calculations using plane wave methods. As discussed in Section 1.2.2, this required the use of a large supercell (16 Å) with a "zigzag" shaped applied potential [55]. This system is an ideal test case for applying the finite field with mixed boundary conditions real space method to the prospect of band gap engineering.

3.2.1.1 Computational Details

Our calculations were performed using Ceperley and Alder's formulation of the LDA exchange correlation potential [7]. The carbon pseudopotential was generated according to the scheme of Troullier and Martins [9] with cutoff radii of 1.49 and 1.52 a_0 for the 2s and 2p orbitals. A bond length of 1.406 Å was found to minimize in plane forces below 10^{-5} Ry/a_0, in excellent agreement with experimental values for graphite [56]. The interplanar distance was not relaxed as it is strongly dependent on long range van der Waals interactions which are not observed in DFT [57]. Instead the interplanar distance was fixed at 3.35 Å as in [55]. A grid spacing of 0.25 a_0 was chosen, and a 19 $\times$ 19 Monkhorst-Pack grid was used to sample k points [14].

To determine the necessary amount of vacuum space, the Clausius Mossotti polarizability (Equation 3.3) was calculated as a function of the amount of space. As the polarizability is a measure of how freely a volume of electrons moves in response to an applied field, this make it sensitive to any

pinning or distortion of the wave functions due to the boundary conditions. Figure 3.2 illustrates the results. At 13.7 a_0, the polarizability is completely converged. Accounting for the space between sheets, this 13.7 a_0 is equivalent to a supercell of 10.6 Å in depth.

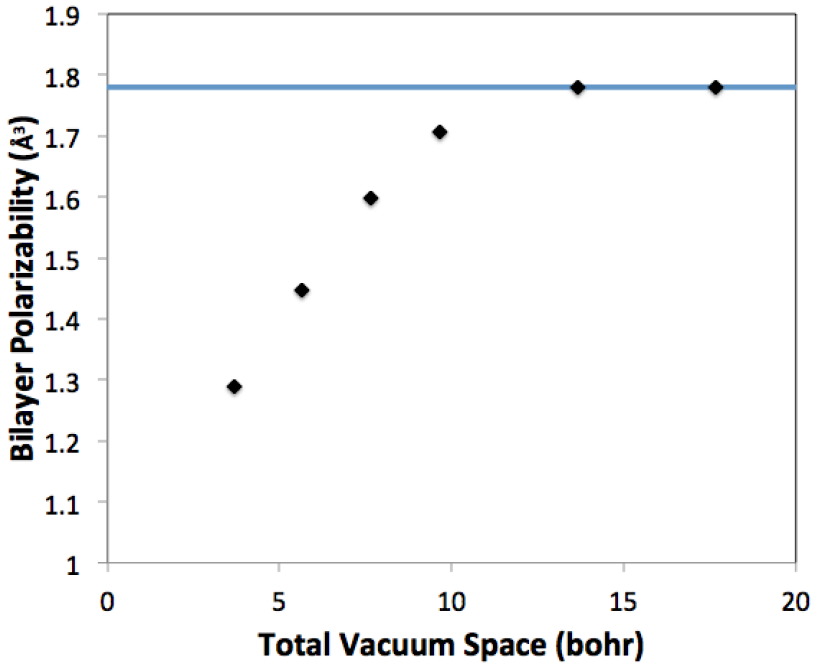

Figure 3.2: The polarizability of bilayer graphene in Å^3 as a function of the total vacuum space in a.u. Total vacuum space is counted as the sum of the distances from the positive z axis boundary to the highest carbon nucleus and the lowest carbon nucleus to the negative z axis boundary.

3.2.1.2 Results and Discussion

Figure 3.3 shows the calculated band gap in bilayer graphene as a function of the bias voltage due to a transverse electric field. These results are in good agreement with that of Min *et al.* [55] – a gap opens rapidly but then saturates at approximately 0.25 eV as the applied bias voltage approaches

2 volts.

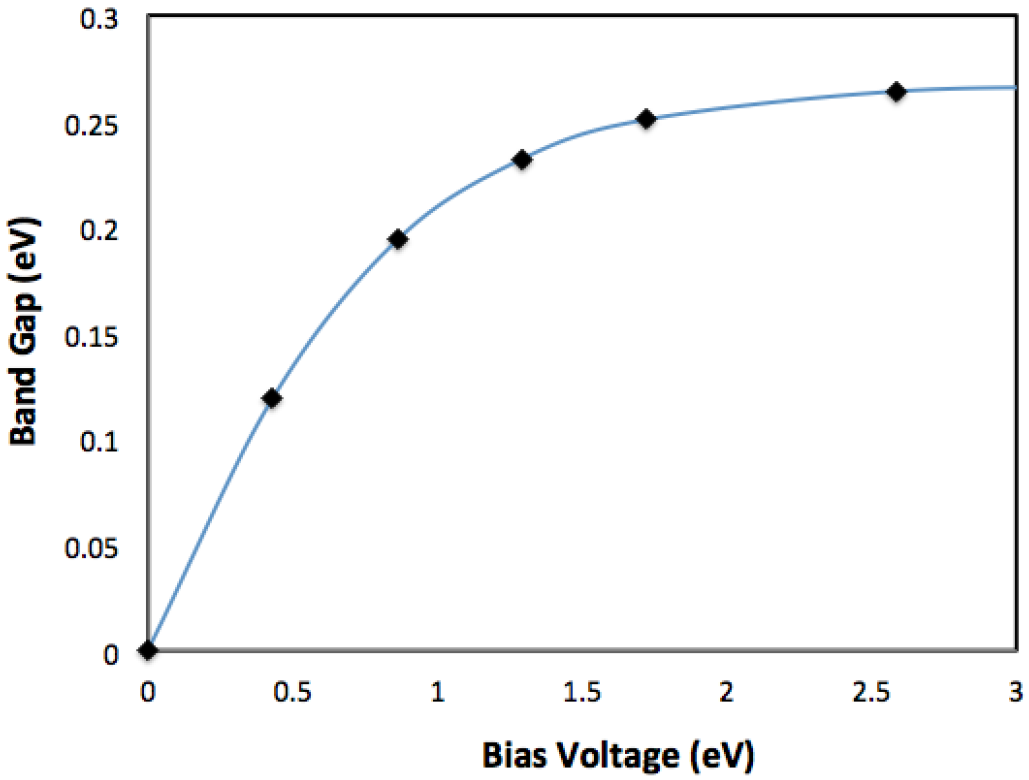

Figure 3.3: The band gap in bilayer graphene as a function of the applied biasing potential between layers.

The nature of the band gap saturation can be seen in Figure 3.5 which plots the band structure near the K point for increasing field strengths. As the gap opens, it takes the form of a Mexican hat potential, such that the gap minimum is slightly displaced from the K point. As the field further increases, this structure grows more pronounced such that the valence band maximum and conduction band minimum move farther from the K point while maintaining a similar gap. This behavior is well replicated in both prior tight binding and DFT models [54, 55].

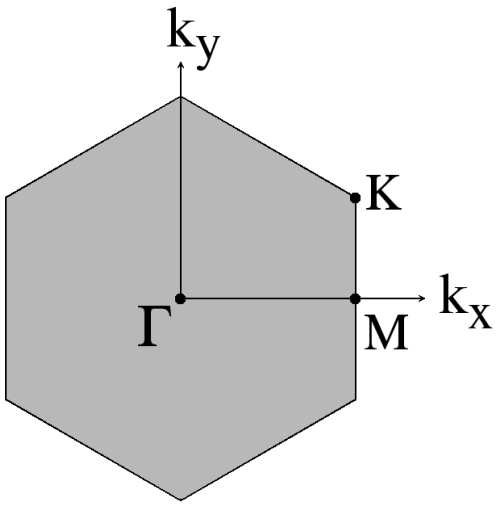

Figure 3.4: Brillouin zone and symmetry points of graphene.

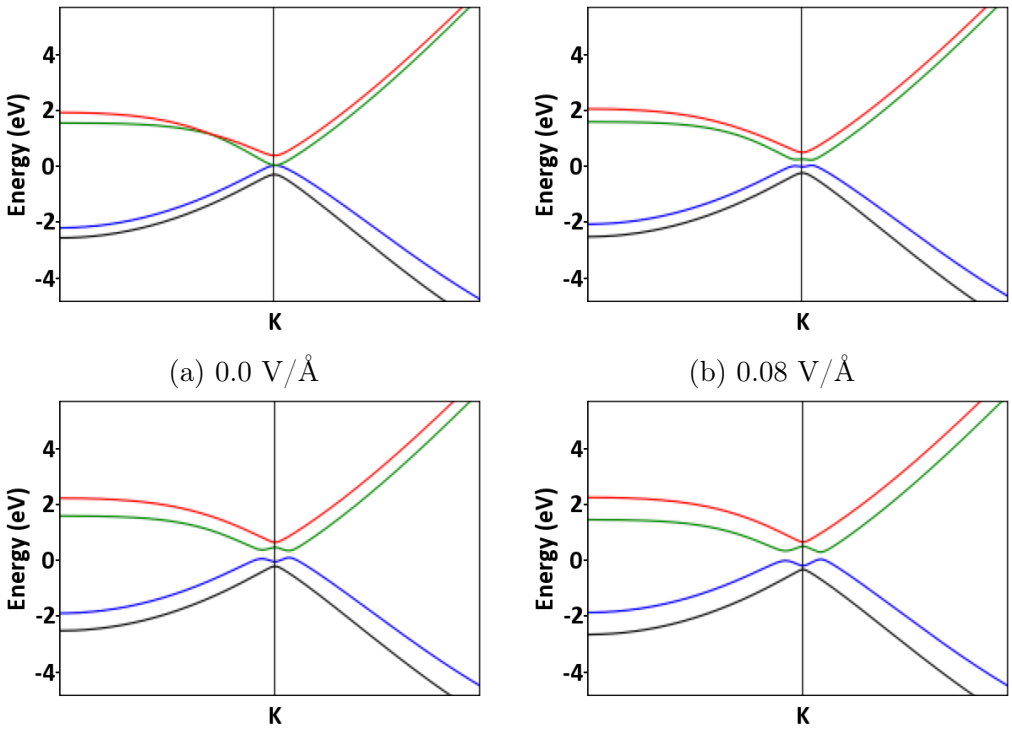

(a) 0.0 V/Å

(b) 0.08 V/Å

(c) 0.16 V/Å

(d) 0.24 V/Å

Figure 3.5: Band structure of bilayer graphene near the K point for increasing applied fields.

These results show that real space DFT can capture the critical, qualitative changes in band structure necessary for investigating new materials for engineering tunable band gaps.

3.2.2 Modifying the Gap in Phospherene and Analogues

There are many more materials besides graphene that can be exfoliated to yield single or few molecular layer sheets. For example, transition metal dichalcogenides such as MoS_2, like graphene, can be exfoliated to produce molecularly thin layers. Unlike graphene, MoS_2 has a band gap of 1.2 eV, which is an indirect gap in bulk form. The gap increases to a 1.8 eV direct gap in the monolayer form. Studies show that the band gap of the bilayer form can be controlled by the application of a transverse electric field [58]. The fields necessary, however, are enormous, of the order 1 V/Å to significantly close the gap. This raised the possibility that there are other 2D materials that might have even more practical tunable band gaps.

Black phosphorus, also known as phosphorene in its monolayer form, is another layered material that exhibits unique properties. As with graphene, layers just a few molecules thick can be mechanically exfoliated from the bulk form by peeling them off with tape [59, 60]. Structurally, the layers take a puckered configuration seen in Figure 3.6 that is mechanically flexible [61]. The band gap occurs near the Γ point and is extremely anisotropic as seen in Figure 3.7. While the valence band takes an approximately parabolic shape near the Γ point in the X direction, it is nearly flat in the Y direction. Previous work has shown the band gap in phosphorene is sensitive to mechanical strain

and electric fields [62–64]. Li *et al.* reported that the gap in monolayer phosphorene closes around 1.3 V/Å. Further theoretical and experimental work has demonstrated more sensitive band gap tuning in few layer phosphorene, an effect referred to as the giant Stark effect [59, 65–68].

Phosphorus is a group V element with 5 valence electrons per atom. The combination of group IV elements with chalcogenides yields many new species isoelectronic to phosphorene. A number of these group IV monochalcogenides have been observed or are predicted to have a buckled structure analogous to phosphorene [69]. We utilize real-space pseudopotential DFT to investigate the effects of transverse electric fields on few layer phosphorene and its group IV monochalcogenide analogues GeS, GeSe, SnS, and SnSe.

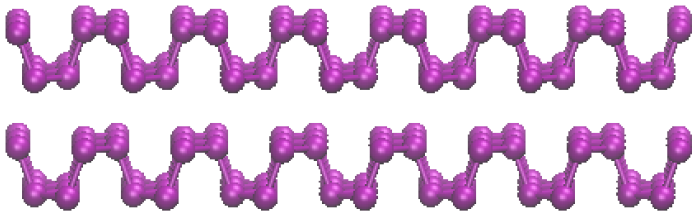

Figure 3.6: Illustration of the puckered structure of phosphorene layers.

3.2.2.1 Computational Details

The calculations were performed using the exchange correlation functional proposed by Perdew, Burke, and Ernzerhof (PBE), a generalized gradient approximation (GGA) method [70]. This functional was chosen over LDA so that calculations could be directly compared to a number of previous theoretical results. Troullier Martins pseudopotentials were generated according to the parameters found in Table 3.1.

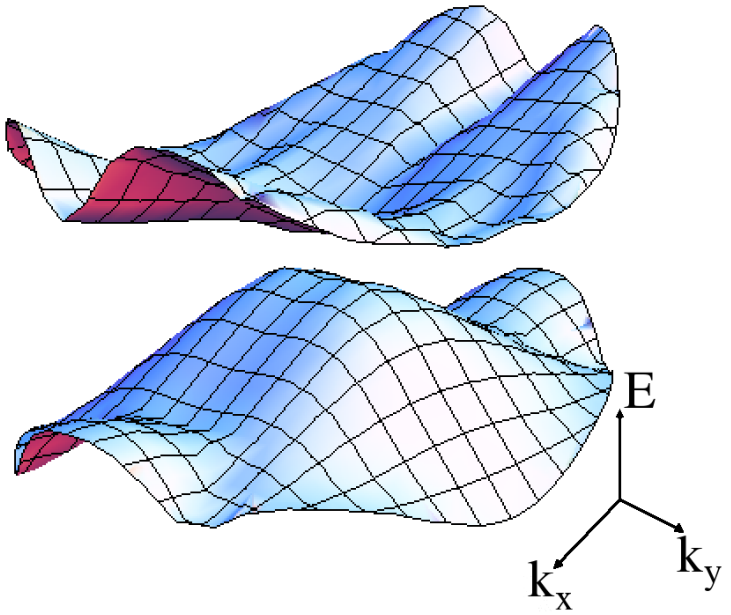

Figure 3.7: Plot of the highest valence and lowest conduction bands near the Γ point for Phosphorene, illustrating the unique anisotropic structure.

Grid spacings of approximately 0.25 a_0 (adjusted to fit the unit cell dimensions) were used. Along the non-periodic z axis, 8 a_0 of vacuum space was included between the nuclei and boundary. The band structures of phosphorene and GeS depend strongly on strain [62, 64, 71]. All structures were optimized to reduce the residual Hellman-Feynman forces below 10^{-3} Ryd/a_0.

In the multilayer systems, the interlayer interaction is dominated by long range van der Waals (vdW) forces that are not captured by GGA DFT calculations. To properly account for this effect during geometry optimization, the dispersion correction method proposed by Tkatchenko and Scheffler is utilized [57]. This method models uses the DFT charge density to determine interatomic coefficients and does not rely on empirical parameters.

The Brillouin zone is sampled using the Monkhorst-Pack scheme [14]. A

Table 3.1: Pseudopotential configurations with cutoff radii in a_0.

Atom	Configuration	s-cutoff	p-cutoff	d-cutoff	Local comp.
P	[Ne] $3s^2$ $3p^3$	1.70	1.88	2.00	s
Ge	[Ar $3d^{10}$] $4s^2$ $4p^2$	2.06	2.85	2.58	p
Sn	[Kr $4d^{10}$] $5s^2$ $5p^2$	2.40	2.46	2.79	p
S	[Ne] $3s^2$ $3p^4$	1.61	1.76	1.92	p
Se	[Ar $3d^{10}$] $4s^2$ $4p^4$	1.94	2.11	1.94	p

Γ centered grid of 14×14 points was utilized for band structure calculations.

3.2.2.2 Structural Results

Phosphorene and its electronic analogues, the group IV monochalcogenides have orthrhombic unit cells with a unique puckered layer structure. Singh and Hennig have predicted that this structure remains dynamically stabile when isolated to the monolayer [69]. Figure 3.8 illustrates this structure for bilayer GeS. The individually optimized lattice parameters for all systems are presented in Table 3.2.

Lattice parameters are not found to vary significantly between mono-, bi-, and trilayer systems. Furthermore, the long axis of the unit cell only varies by about 6% across species. The short axis is more responsive to the size of the constituent atoms and varies from 3.30 Å for phosphorene to 4.33 Å for SnSe. We find a similar trend as observed by Fei et al. [72]. The lattice parameter **a** increases with number of layers while lattice parameter **b** decreases. This trend holds for GeSe, SnS, and SnSe . Figure 3.9 shows the similarities between structures for bilayers of all species.

Table 3.2: Relaxed cell sizes for one, two, and three layer systems in Å, compared to bulk experiment

	Monolayer		Bilayer		Trilayer		Bulk Expt.	
	a	**b**	**a**	**b**	**a**	**b**	**a**	**b**
P	4.56	3.30	4.49	3.31	4.47	3.30	4.38	3.31[a]
GeS	4.46	3.69	4.37	3.67	4.41	3.68	4.31	3.64[b]
GeSe	4.28	4.00	4.34	3.97	4.37	3.94	4.39	3.84[c]
SnS	4.29	4.10	4.36	4.09	4.40	4.08	4.33	3.99[d]
SnSe	4.41	4.33	4.47	4.26	4.49	4.25	4.44	4.15[d]

[a] [73, 74], [b] [75], [c] [76], [d] [77–79]

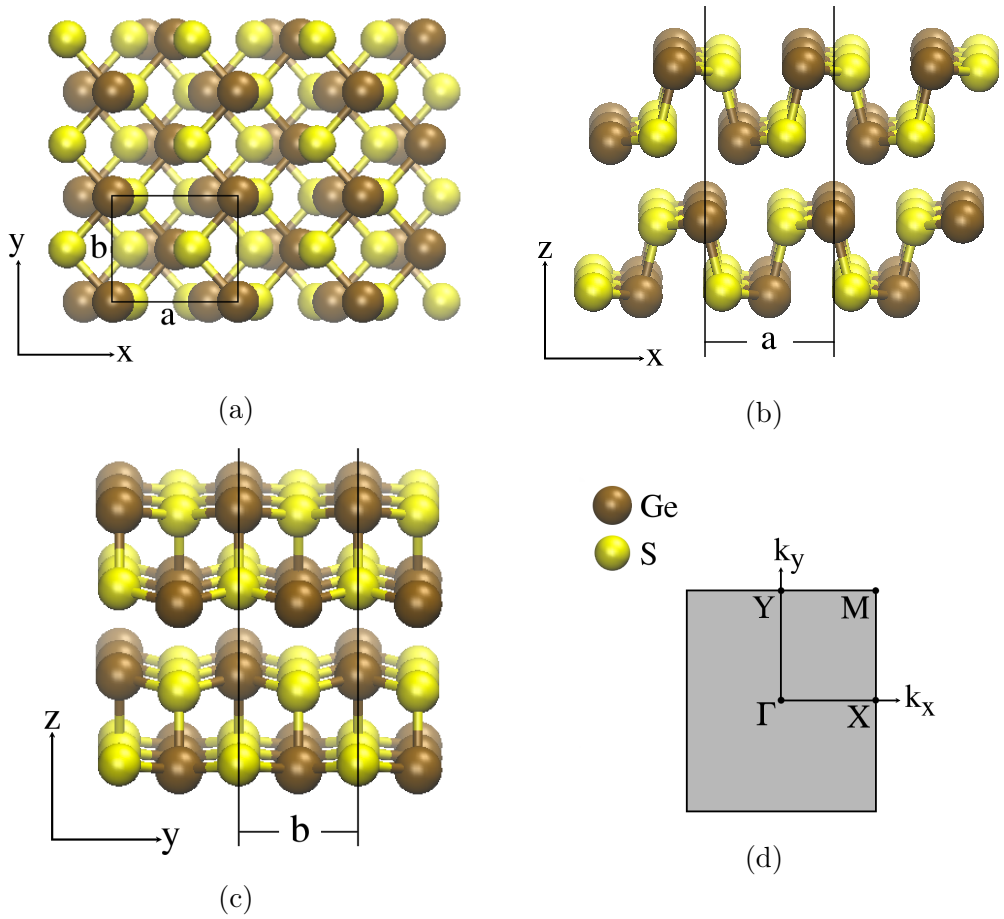

Figure 3.8: (a) – (c) Orthographic projections of bilayer GeS crystal structure and (d) symmetry points of Brillouin zone.

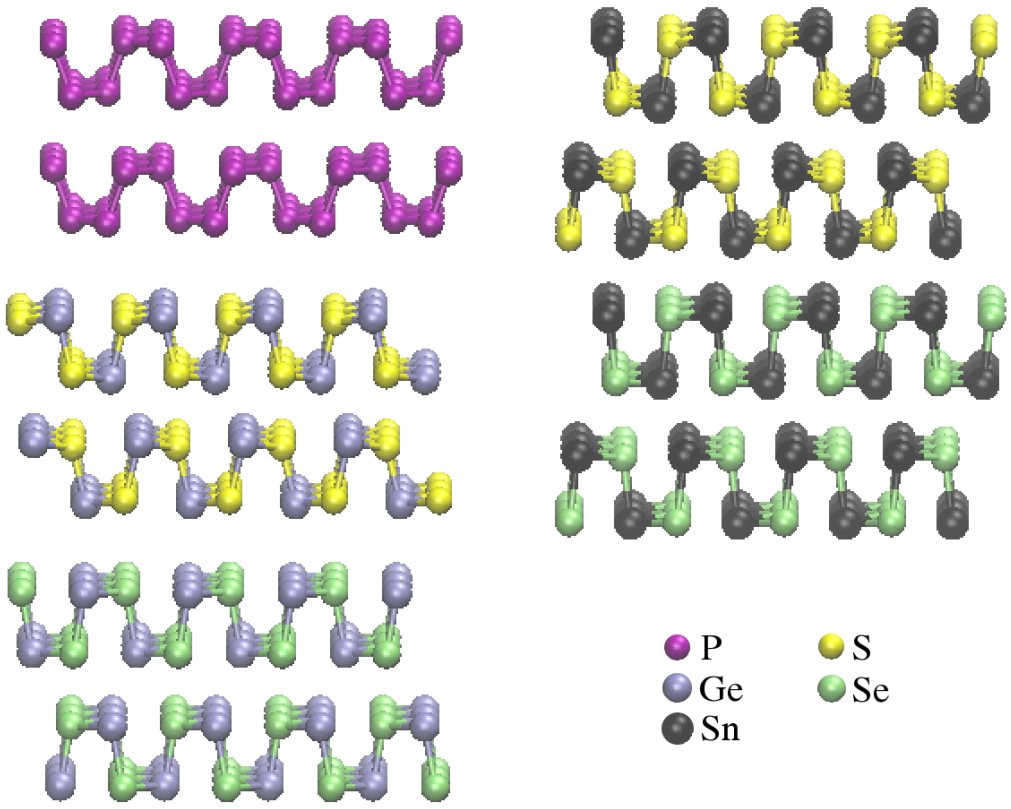

Figure 3.9: Bilayer structures for phosphorene and analogues (all crystals sizes to scale).

Optimization of the structure requires we calculate the total energy as a function of the lattice parameters. We then also find information about the elastic stiffness of these layered systems. For a 2D system the stiffness coefficients are given by:

$$C_{ij} = \frac{1}{A_0}\frac{\partial^2 U}{\partial \varepsilon_{ii} \partial \varepsilon_{jj}} \tag{3.6}$$

where A_0 is the relaxed unit-cell area, U is the total energy per unit-cell, and ε_{ii} is strain along the i^{th} axis defined by the fractional change in lattice parameter $(l - l_0)/l_0$ [72].

The calculated stiffness coefficients C_{11} and C_{22} are presented in Table 3.3 and compared to prior theoretical calculations. As ε_{ii} is dimensionless, the coefficients in (3.6) have SI units J/m^2 or N/m. Wei *et al.* [61] and Gomes *et al.* [80] list monolayer elasticities in N/m^2 for easier comparison to bulk values, in which case the nominal thickness d_0 given by the interlayer spacing is used as a conversion factor.

As is seen in Table 3.3, there is significant disagreement in the literature over the stiffness of the group IV monochalcogenides, even though the listed sources are all theoretical calculations at the same level of theory (DFT with PBE functional) – reported stiffnesses vary by up to a factor of two. Our calculations fall within the reported range, but do not coincide with any one reported set of data.

As with phosphorene, the group IV monochalcogenides are highly anisotropic. Deformations along the x axis flatten the puckered structure (see Figure 3.8b) rather than change bond lengths. The stiff axes of the group IV monochalcogenides are more than twice as soft as the corresponding phosphorene axis,

Table 3.3: Calculated monolayer elastic coefficients in N/m.

	Calculated		Previous Theory	
	C_{11}	C_{22}	C_{11}	C_{22}
P	18	101	24[a]	92[a]
GeS	13	44	15[b,c]–20[d]	33[b]–53[d]
GeSe	20	47	12[b]–24[c]	30[b]–50[c]
SnS	20	42	14[b,d]–21[c]	26[b]–43[c]
SnSe	24	43	11[b]–20[d]	25[b]–44[d]

[a] [61] with monolayer thickness of 5.55 Å, [b] [82], [c] [80], [d] [72]

and much softer than other common 2D materials such as MoS_2 which has $C_{11} = C_{22} = 130$ N/m [81].

3.2.2.3 Electronic Results

The calculated band gaps for all systems are summarized in Table 3.4. Excellent agreement is found for the monolayer gap with literature values performed at the same level of theory (GGA DFT) [64, 82]. The band structures for each system can be found in Figures 3.10, 3.11, and 3.12.

Table 3.4: Band gaps of phosphorene and analogues in eV compared with literature values for the monolayer.

	Monolayer	Bilayer	Trilayer	Monolayer Lit.
P	0.75*	0.43*	0.20*	0.7[a]
GeS	1.73	1.37*	1.31	1.73[b]
GeSe	1.13*	0.96*	0.91*	1.17[b]
SnS	1.41	0.86	0.75	1.46[b]
SnSe	0.90*	0.77	0.69	1.00[b]

[a] [64], [b] [82], * direct or nearly direct gap

The unperturbed band structures have several notable features. In

Table 3.5: Locations of the valence band maxima and conduction band minima relative to the Γ point in units of (2π/a, 2π/b).

	Monolayer	Bilayer	Trilayer
P VBM	(0.00, 0.07)	(0.00, 0.00)	(0.00, 0.07)
P CBM	(0.00, 0.00)	(0.00, 0.00)	(0.00, 0.00)
GeS VBM	(0.00, 0.00)	(0.00, 0.00)	(0.00, 0.00)
GeS CBM	(0.00, 0.79)	(0.00, 0.00)	(0.00, 0.65)
GeSe VBM	(0.80, 0.00)	(0.75, 0.00)	(0.75, 0.00)
GeSe CBM	(0.80, 0.00)	(0.80, 0.00)	(0.80, 0.00)
SnS VBM	(0.75, 0.00)	(1.00, 0.00)	(0.95, 0.00)
SnS CBM	(0.00, 0.80)	(0.00, 0.71)	(0.00, 0.67)
SnSe VBM	(0.80, 0.00)	(0.85, 0.00)	(0.90, 0.00)
SnSe CBM	(0.80, 0.00)	(0.00, 0.70)	(0.00, 0.67)

monolayer phosphorene, the conduction band minimum (CBM) occurs at the Γ point, while the valence band maximum (VBM) is slightly displaced towards the Y point (the conduction band at the Γ point is within 2 meV of the CBM). The dispersion is highly anisotropic, with the conduction band being nearly constant along the Γ - X axis near Γ. This character remains for bilayer and trilayer phosphorene, though the gap shrinks considerably. The calculated trilayer gap at 0.20 eV is already smaller than the experimental bulk gap of 0.35 eV [83].

While the group IV monochalcogenides are structurally very similar to phosphorene, significant differences are observed in their band structures. Overall, the group IV monochalcogenides display more isotropic dispersion, and have multiple valence band maxima and conduction band minima along the Γ-X and Γ-Y axes.

The GeS monolayer has an indirect gap with the VBM located at the Γ point while the CBM resides close to the Y point. In bilayer form, the CBM

moves to the Γ point, but reverts back towards the Y point for the trilayer system. The locations of all VBM and CBM relative to the Γ point are listed in Table 3.5.

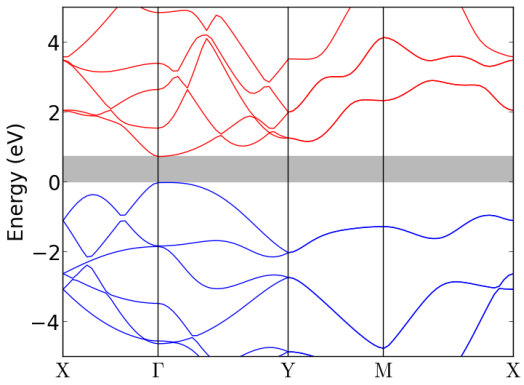

(a) Monolayer phosphorene

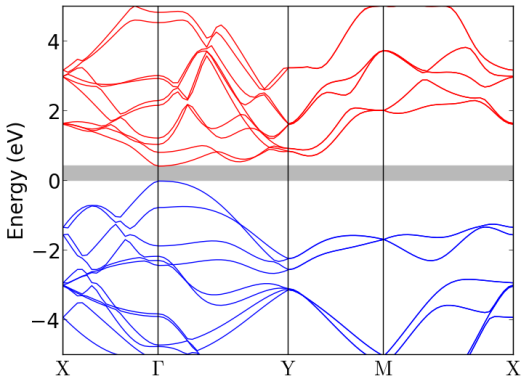

(b) Bilayer phosphorene

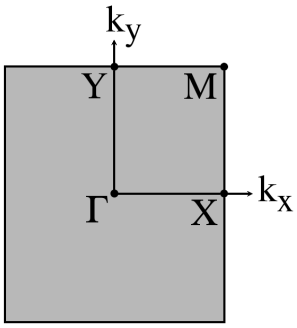

(d)

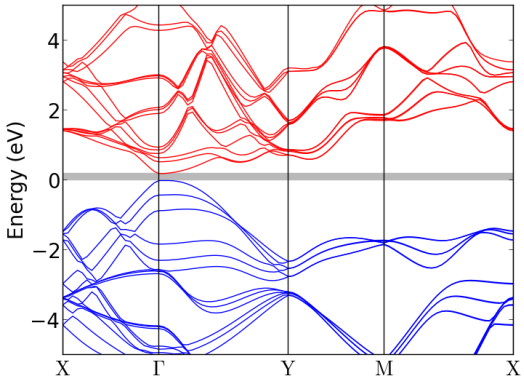

(c) Trilayer phosphorene

Figure 3.10: Plots of the band structure of (a) monolayer, (b) bilayer, and (c) trilayer phosphorene with symmetry points of the Brillouin zone illustrated in (d).

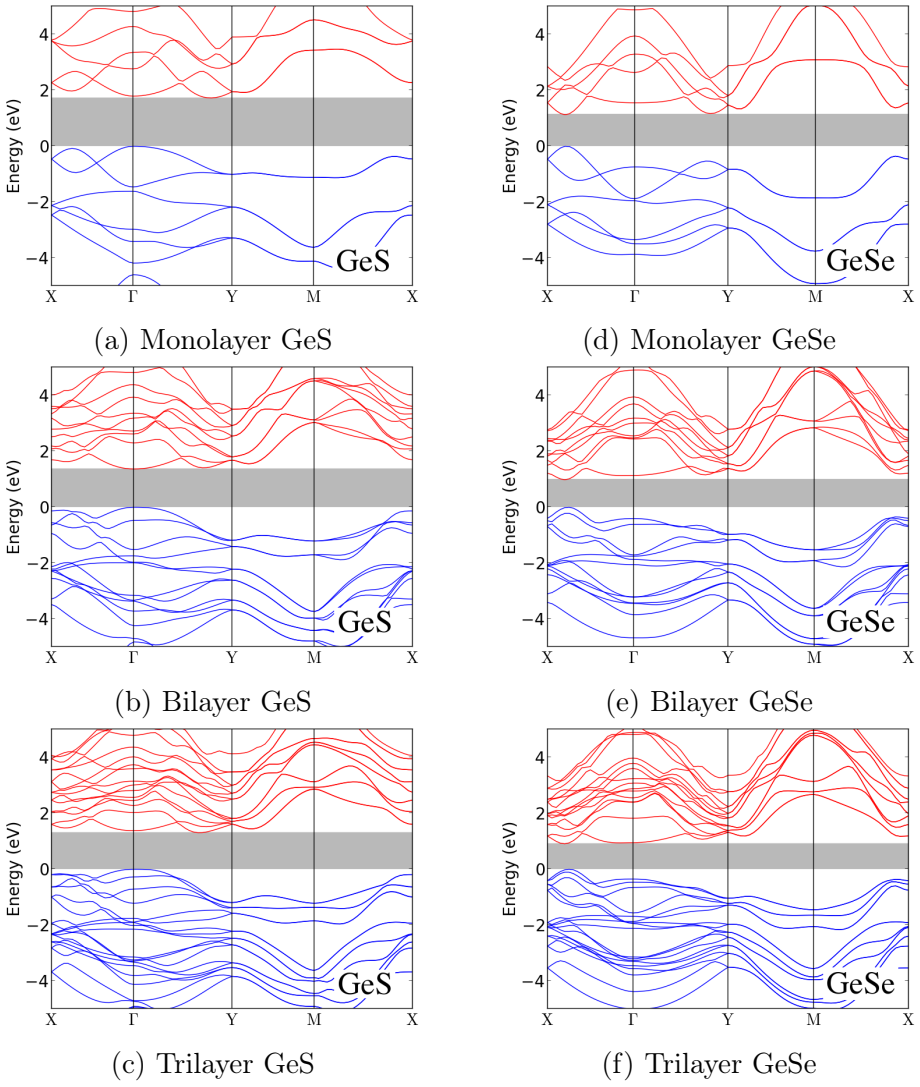

(a) Monolayer GeS

(d) Monolayer GeSe

(b) Bilayer GeS

(e) Bilayer GeSe

(c) Trilayer GeS

(f) Trilayer GeSe

Figure 3.11: Band structures of monolayer, bilayer, and trilayer GeS (a – c) and GeSe (d – f).

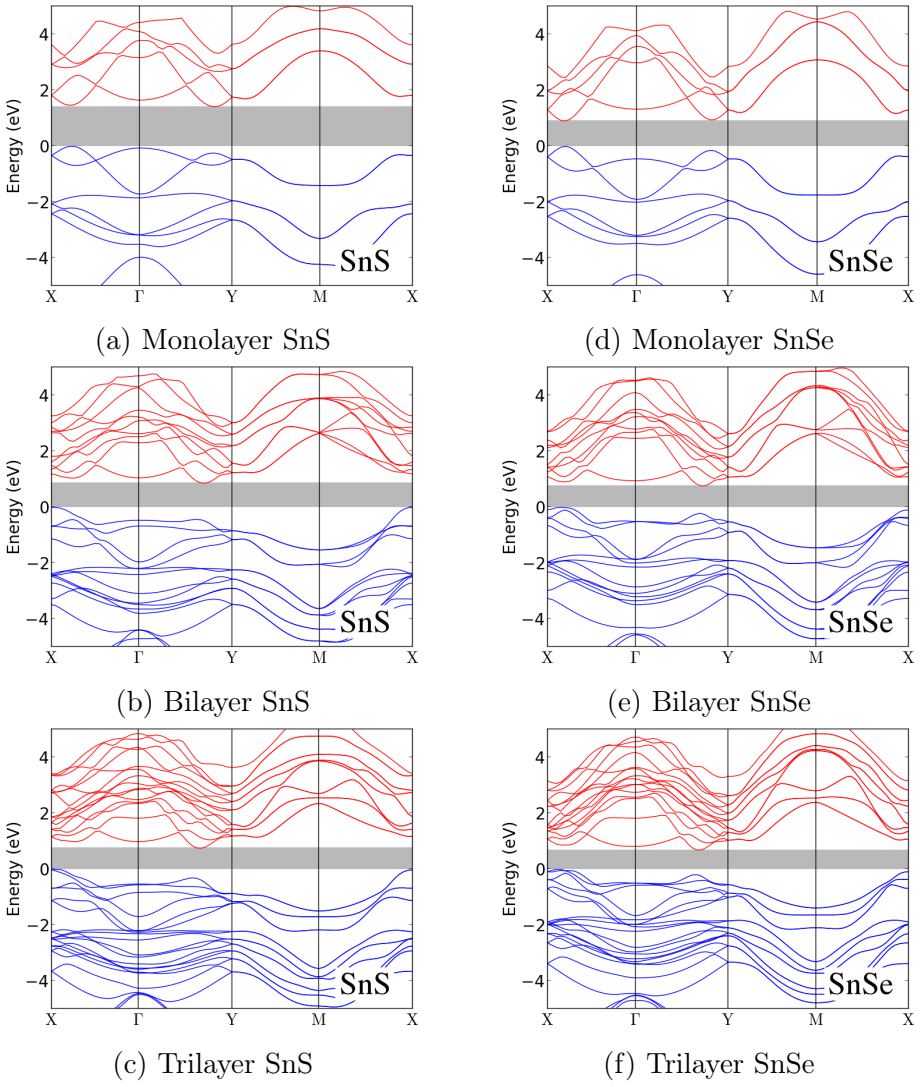

(a) Monolayer SnS (d) Monolayer SnSe

(b) Bilayer SnS (e) Bilayer SnSe

(c) Trilayer SnS (f) Trilayer SnSe

Figure 3.12: Band structures of monolayer, bilayer, and trilayer SnS (a – c) and SnSe (d – f).

The band gap of phosphorene is known to be sensitive to the application of a transverse electric field [62, 65]. We plot the calculated effect of electric fields on the band gaps of phosphorene and the group IV monochalcogenides in Figure 3.13. The band gap of bilayer phosphorene is found to be much more sensitive to the applied field than the monolayer. In the limit of non-interacting layers, this can be understood as the electric field breaking the degeneracy between bands in different layers. This can be seen in Figure 3.14 where the monolayer bands are nearly unperturbed by electric fields sufficient to collapse the gap in bilayer phosphorene. The energy difference between the first and second conduction bands at Γ grows linearly with the field.

The results for bilayer group IV monochalcogenides are broadly similar – band gaps steadily decrease under applied field until collapsing between 0.13 and 0.20 V/Å. However, the group IV monochalcogenides have much larger band gaps than bilayer phosphorene, indicating the giant Stark effect is even stronger here. In terms of the average reduction in band gap per unit field strength, bilayer phosphorene yields 2.5 eV/(V/Å) which is less than half the response of bilayer GeS: 6.8 eV/(V/Å). This represents a significant increase in the range of band gaps that could be selected in novel gated optoelectronics as suggested by Liu *et al.* [65].

The monolayer group IV selenides show entirely new behavior under fields – up until approximately 0.15 V/Å the band gap responds only neglibly to the applied field. After 0.15 V/Å, the band gap drops precipitously at approximately 10 eV/(V/Å). Figure 3.15 illustrates how this happens. With no field applied, monolayer GeSe is a direct gap semiconductor with CBM

and VBM near X. The CB at Γ is associated with the vertically oriented p_z orbitals. As this state is localized by the field, the CB at Γ steadily decreases in energy while the rest of the band structure remains largely unchanged. At approximately 0.15 V/Å, the CB at Γ overtakes the original CBM, turning the monolayer into an indirect semiconductor. As the field continues to grow, the CB at Γ continues to fall, leading to a linear reduction in band gap until the material becomes a semimetal. The critical field to drive the semiconductor-metallic transition is 0.28 V/Å for monolayer GeSe and 0.22 V/Å for SnSe.

The giant Stark effect coefficient is defined by $S_L = -(\Delta E_g/\Delta E_{field})/e$ [65]. The average coefficients for the group IV monochalcogenides are listed in Table 3.6. The Stark coefficients for these materials are comparable or greater than reported values of ∼3 Å for 4 layer phosphorene [68].

Table 3.6: Giant Stark effect coefficients for group IV monochalcogenides in Å.

	Monolayer	Bilayer	Trilayer
GeS	6.2	6.8	8.5
GeSe	4.1	5.1	8.0
SnS	5.1	5.4	6.0
SnSe	4.1	5.7	6.9

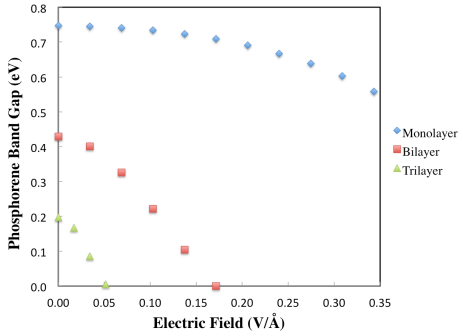

(a) Phosphorene

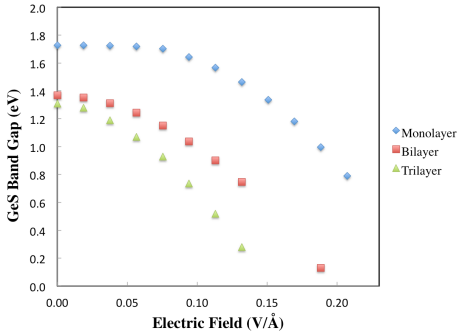

(b) GeS

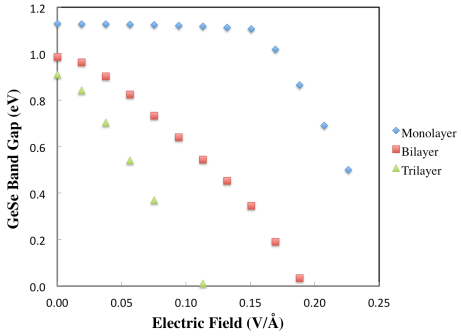

(d) GeSe

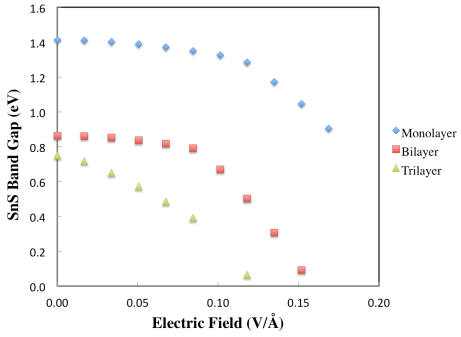

(c) SnS

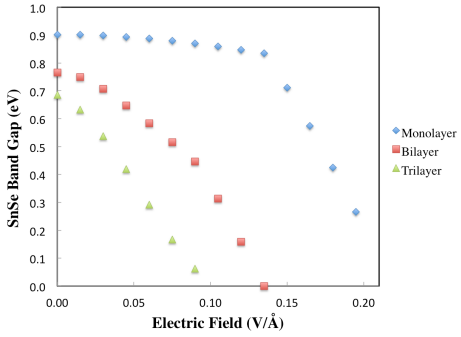

(e) SnSe

Figure 3.13: Band gaps for phosphorene and analogues as a function of electric field.

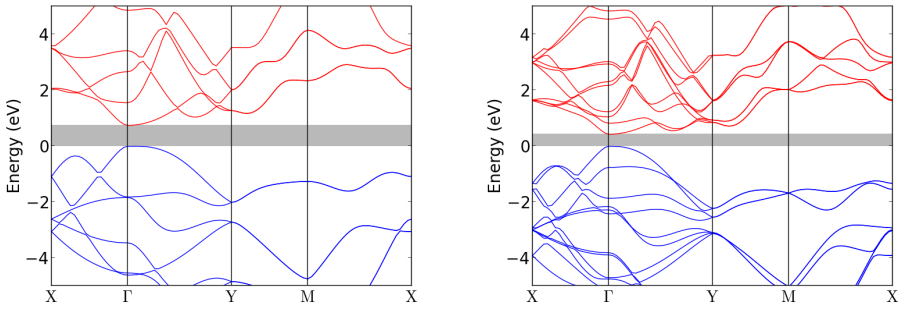

(a) Monolayer at 0.000 V/Å

(e) Bilayer at 0.000 V/Å

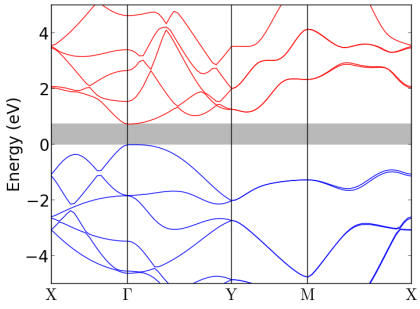

(b) Monolayer at 0.069 V/Å

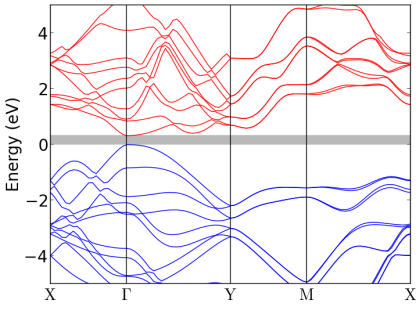

(f) Bilayer at 0.069 V/Å

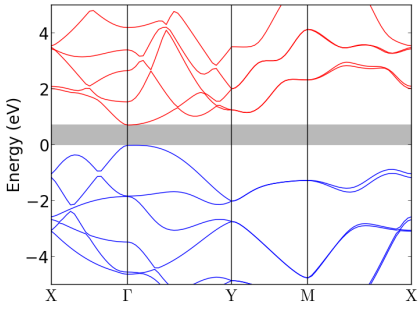

(c) Monolayer at 0.137 V/Å

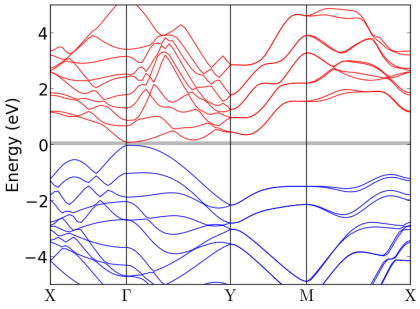

(g) Bilayer at 0.137 V/Å

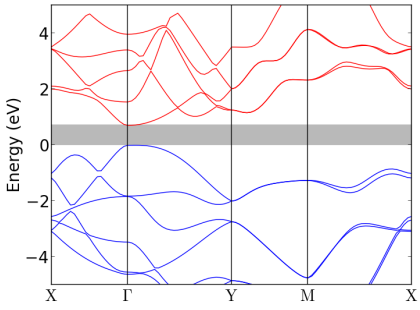

(d) Monolayer at 0.172 V/Å

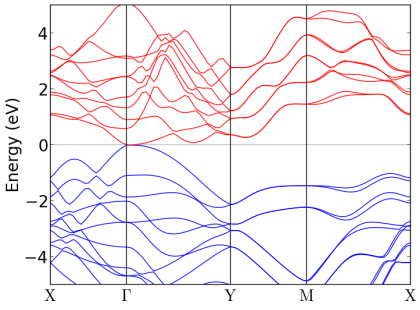

(h) Bilayer at 0.172 V/Å

Figure 3.14: Comparison of the band structures of monolayer and bilayer phosphorene under applied fields.

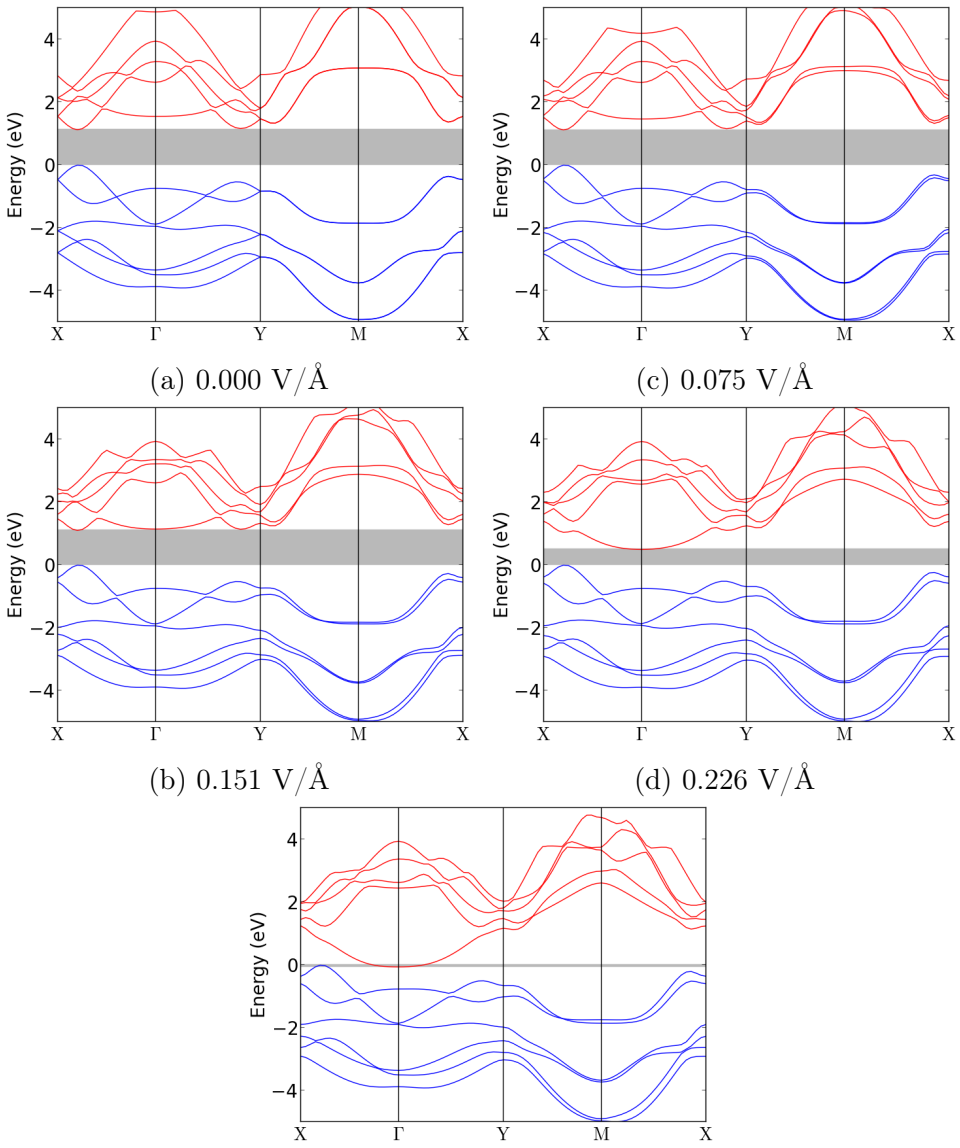

(a) 0.000 V/Å

(c) 0.075 V/Å

(b) 0.151 V/Å

(d) 0.226 V/Å

(e) 0.283 V/Å

Figure 3.15: Band structure of monolayer GeSe under applied fields showing the transition from direct gap semiconductor to indirect gap semiconductor to semimetal.

3.2.3 Discussion

We have used real space density functional theory with pseudopotentials to calculate the response of few layer phosphorene and its group IV monochalcogenide analogues to external transverse fields. We find the giant Stark effect causes the band gaps of these materials to be highly sensitive to the applied field. As multilayer group IV monochalcogenide systems have significantly larger band gaps than multilayer phosphorene systems, this increases the range of possible band gap tunable devices.

Bibliography

[1] S. D. Dalosto, J. M. Vanderkooi, and K. A. Sharp, "Vibrational stark effects on carbonyl, nitrile, and nitrosyl compounds including heme ligands, CO, CN, and NO, studied with density functional theory," *J. Phys. Chem. B*, vol. 108, no. 20, pp. 6450–6457, 2004.

[2] J. R. Chelikowsky, "The pseudopotential-density functional method applied to nanostructures," *J. Phys. D: Appl. Phys.*, vol. 33, pp. R33–R50, January 2000.

[3] Y. Saad, Y. Zhou, C. Bekas, M. L. Tiago, and J. Chelikowsky, "Diagonalization methods in PARSEC," *Phys. Stat. Sol. B*, vol. 243, no. 9, pp. 2188–2197, 2006.

[4] L. Kronik, A. Makmal, M. L. Tiago, M. M. G. Alemany, M. Jain, X. Huang, Y. Saad, and J. R. Chelikowsky, "PARSEC – the pseudopotential algorithm for real-space electronic structure calculations: recent advances and novel applications to nano-structures," *Phys. Status Solidi B*, vol. 243, no. 5, pp. 1063–1079, 2006.

[5] W. Kohn and L. J. Sham, "Self-consistent equations including exchange and correlation effects," *Phys. Rev.*, vol. 140, pp. A1133–A1138, November 1965.

[6] W. R. Burdick, Y. Saad, L. Kronik, I. Vasiliev, M. Jain, and J. R. Chelikowsky, "Parallel implementation of time-dependent density functional theory," *Comp. Phys. Comm.*, vol. 156, pp. 22–42, 2003.

[7] D. M. Ceperley and B. J. Alder, "Ground state of the electron gas by a stochastic method," *Phys. Rev. Lett.*, vol. 45, pp. 566–569, August 1980.

[8] J. A. Bearden and A. F. Burr, "Reevaluation of x-ray atomic energy levels," *Rev. Mod. Phys.*, vol. 39, pp. 125–142, January 1967.

[9] N. Troullier and J. L. Martins, "Efficient pseudopotentials for plane-wave calculations," *Phys. Rev. B*, vol. 43, pp. 1993–2006, January 1991.

[10] L. Kleinman and D. M. Bylander, "Efficacious form for model pseudopotentials," *Phys. Rev. Lett.*, vol. 48, no. 20, p. 1425, 1982.

[11] Y. Zhou, Y. Saad, M. L. Tiago, and J. R. Chelikowsky, "Self-consistent-field calculations using Chebyshev-filtered subspace iteration," *J. Comp. Phys.*, vol. 219, pp. 172–184, 2006.

[12] Y. Zhou, Y. Saad, M. Tiago, and J. R. Chelikowsky, "Parallel self-consistent-field calculations via Chebyshev-filtered subspace acceleration," *Phys. Rev. E*, vol. 74, p. 066704, 2006.

[13] K. H. Khoo, M. Kim, G. Schofield, and J. R. Chelikowsky, "Ab initio molecular dynamics simulations using a chebyshev-filtered subspace iteration technique," *Phys. Rev. B*, vol. 82, p. 064201, 2010.

[14] H. J. Monkhorst and J. D. Pack, "Special points for Brillouin-zone integrations," *Phys. Rev. B*, vol. 13, no. 12, pp. 5188–5192, 1976.

[15] P. P. Ewald, "Die Berechnung optischer und elektrostatischer Gitterpotentiale," *Ann. Phys.*, vol. 369, pp. 253–287, 1921.

[16] X. Blase, A. Rubio, S. G. Louie, and M. L. Cohen, "Mixed-space formalism for the dielectric response in periodic systems," *Phys. Rev. B*, vol. 52, no. 4, pp. R2225–R2228, 1995.

[17] A. Natan, A. Benjamini, D. Naveh, L. Kronik, M. L. Tiago, S. P. Beckman, and J. R. Chelikowsky, "Real-space pseudopotential method for first principles calculations of general periodic and partially periodic systems," *Phys. Rev. B*, vol. 78, p. 075109, 2008.

[18] I. Vasiliev, S. Öğüt, and J. R. Chelikowsky, "Ab initio calculations for the polarizabilities of small semiconductor clusters," *Phys. Rev. Lett.*, vol. 78, pp. 4805–4808, June 1997.

[19] I. T. Suydam, C. D. Snow, V. S. Pande, and S. G. Boxer, "Electric fields at the active site of an enzyme: Direct comparison of experiment with theory," *Science*, vol. 313, pp. 200–204, July 2006.

[20] A. T. Fafarman and S. G. Boxer, "Nitrile bonds as infrared probes of electrostatics in Ribonuclease S," *J. Phys. Chem. B*, vol. 114, no. 42, pp. 13536–13544, 2010.

[21] L. N. Silverman, M. E. Pitzer, P. O. Ankomah, S. G. Boxer, and E. E. Fenlon, "Vibrational stark effect probes for nucleic acids," *J. Phys. Chem. B*, vol. 111, no. 40, pp. 11611–11613, 2007.

[22] N. M. Levinson, E. E. Bolte, C. S. Miller, S. A. Corcelli, and S. G. Boxer, "Phosphate vibrations probe local electric fields and hydration in biomolecules," *J. Am. Chem. Soc.*, vol. 133, pp. 13236–13239, 2011.

[23] E. S. Park, S. S. Andrews, R. B. Hu, and S. G. Boxer, "Vibrational stark spectroscopy in proteins: A probe and calibration for electrostatic fields," *J. Phys. Chem. B*, vol. 103, no. 45, pp. 9813–9817, 1999.

[24] E. S. Park, M. R. Thomas, and S. G. Boxer, "Vibrational stark spectroscopy of NO bound to heme: Effects of protein electrostatic fields on the no stretch frequency," *J. Am. Chem. Soc.*, vol. 122, no. 49, pp. 12297–12303, 2000.

[25] G. Schkolnik, J. Salewski, D. Millo, I. Zebger, S. Franzen, and P. Hildebrandt, "Vibrational stark effect of the electric-field reporter 4-mercaptobenzonitrile as a tool for investigating electrostatics at electrode/sam/solution interfaces," *Int. J. Mol. Sci.*, vol. 13, pp. 7466–7482, 2012.

[26] D. K. Lambert, "Vibrational stark effect of adsorbates at electrochemical interfaces," *Electrochim. Acta*, vol. 41, no. 5, pp. 623–630, 1996.

[27] M. J. Weaver, "Electrostatic-field effects on adsorbate bonding and structure at metal surfaces: parallels between electrochemical and vacuum systems," *Appl. Surf. Sci.*, vol. 67, pp. 147–159, 1993.

[28] S. Sowlati-Hashjin and C. F. Matta, "The chemical bond in external electric fields: Energies, geometries, and vibrational stark shifts of diatomic molecules.," *J. Chem. Phys.*, vol. 139, no. 144101, 2013.

[29] E. S. Park and S. G. Boxer, "Origins of the sensitivity of molecular vibrations to electric fields: carbonyl and nitrosyl stretches in model compounds and proteins," *J. Phys. Chem. B*, vol. 106, pp. 5800–5806, 2002.

[30] J. R. Reimers and N. S. Hush, "Vibrational stark spectroscopy 3. accurate benchmark ab initio and density functional calculations for CO and CN^-," *J. Phys. Chem. A*, vol. 103, no. 49, pp. 10580–10587, 1999.

[31] S. H. Brewer and S. Franzen, "A quantitative theory and computational approach for the vibrational stark effect," *J. Chem. Phys.*, vol. 119, pp. 851–858, July 2003.

[32] D. C. Ferré and J. Niemantsverdriet, "Vibrational stark tuning rates from periodic dft calculations: CO/Pt(1 1 1)," *Electrochim. Acta*, vol. 53, pp. 2897–2906, 2008.

[33] B. F. Garrett, I. Azuri, L. Kronik, and J. R. Chelikowsky, "Real-space pseudopotential method for computing the vibrational Stark effect," *J. Chem. Phys.*, vol. 145, p. 174111, 2016.

[34] S. S. Andrews and S. G. Boxer, "Vibrational stark effects of nitriles i. methods and experimental results," *J. Phys. Chem. A*, vol. 104, pp. 11853–11863, 2000.

[35] J. R. Chelikowsky, N. Troullier, and Y. Saad, "Finite-difference-pseudopotential method: Electronic structure calculations without a basis," *Phys. Rev. Lett.*, vol. 72, pp. 1240–1243, February 1994.

[36] J. R. Chelikowsky, X. Jing, K. Wu, and Y. Saad, "Molecular dynamics with quantum forces: Vibrational spectra of localized systems," *Phys. Rev. B*, vol. 53, no. 18, pp. 12071–12079, 1996.

[37] I. Vasiliev and J. R. Chelikowsky, "Real-space calculations of atomic and molecular polarizabilities using asymptotically correct exchange-correlation potentials," *Phys. Rev. A*, vol. 82, p. 012502, 2010.

[38] L. Kronik, I. Vasiliev, M. Jain, and J. R. Chelikowsky, "Ab initio structures and polarizabilities of sodium clusters," *J. Chem. Phys.*, vol. 115, no. 9, p. 4322, 2001.

[39] K. Parlinski, Z. Q. Li, and Y. Kawazoe, "First-principles determination of the soft mode in cubic ZrO_2," *Phys. Rev. Lett.*, vol. 78, pp. 4063–4066, May 1997.

[40] J. K. Cashion, "Testing of diatomic potential-energy functions by numerical methods," *J. Chem. Phys.*, vol. 39, pp. 1872–1877, October 1963.

[41] D. J. Malik, J. Eccles, and D. Secrest, "On quantal bound state solutions and potential energy surface fitting. a comparison of the finite element, numerov-cooley and finite difference methods," *J. Comput. Phys.*, vol. 38, pp. 157–184, 1980.

[42] N. S. Bobbitt, G. Schofield, C. Lena, and J. R. Chelikowsky, "High order forces and nonlocal operators in a Kohn–Sham hamiltonian," *Phys. Chem. Chem. Phys.*, vol. 17, p. 31542, 2015.

[43] L. Kronik, R. Fromherz, E. Ko, G. Ganteför, and J. R. Chelikowsky, "Highest electron affinity as a predictor of cluster anion structures," *Nat. Mater.*, vol. 1, pp. 49–53, 2002.

[44] D. Beeman, "Some multistep methods for use in molecular dynamics calculations," *J. Comput. Phys.*, vol. 20, pp. 130–139, 1976.

[45] S. Franzen and S. G. Boxer, "Temperature dependence of the electric field modulation of electron-transfer rates: charge recombination in photosynthetic reaction centers," *J. Phys. Chem.*, vol. 97, pp. 6304–6318, February 1993.

[46] L. C. Mayne and B. Hudson, "Resonance Raman spectroscopy of N-methylacetamide: overtones and combinations of the C-N stretch (amide II') and effect of solvation on the C=O stretch (amide I) intensity," *J. Phys. Chem.*, vol. 95, pp. 2962–2967, 1991.

[47] A. K. Geim and I. V. Grigorieva, "Van der waals heterostructures," *Nature*, vol. 499, pp. 419–425, July 2013.

[48] M. Osada and T. Sasaki, "Exfoliated oxide nanosheets: new solution to nanoelectronics," *J. Mater. Chem.*, vol. 19, pp. 2503–25011, March 2009.

[49] Y. Yoon, K. Ganapathi, and S. Salahuddin, "How good can monolayer MoS_2 transistors be?," *Nano Lett.*, vol. 11, pp. 3768–3773, 2011.

[50] E. K. Yu, D. A. Stewart, and S. Tiwari, "Ab initio study of polarizability and induced charge densities in multilayer grapheme films," *Phys. Rev. B*, vol. 77, p. 195406, May 2008.

[51] J. Tóbik and A. D. Corso, "Electric fields with ultrasoft pseudo-potentials: Applications to benzene and anthracene," *J. Chem. Phys.*, vol. 120, pp. 9934–9941, June 2004.

[52] K. S. Novoselov, A. K. Geim, S. V. Morozov, D. Jiang, Y. Zhang, S. V. Dubonos, I. V. Grigorieva, and A. A. Firsov, "Electric field effect in atomically thin carbon films," *Science*, vol. 306, p. 666, October 2004.

[53] E. McCann and V. I. Fal'ko, "Landau-level degeneracy and quantum hall effect in a graphite bilayer," *Phys. Rev. Lett.*, vol. 96, p. 086805, 2006.

[54] E. McCann, "Asymmetry gap in the electronic band structure of bilayer graphene," *Phys. Rev. B*, vol. 74, p. 161403, 2006.

[55] H. Min, B. Sahu, S. K. Banerjee, and A. H. MacDonald, "Ab initio theory of gate induced gaps in graphene bilayers," *Phys. Rev. B*, vol. 75, p. 155115, April 2007.

[56] P. R. Wallace, "The band theory of graphite," *Phys. Rev.*, vol. 71, no. 9, pp. 622–634, 1946.

[57] A. Tkatchenko and M. Scheffler, "Accurate molecular van der Waals interactions from ground-state electron density and free-atom reference data," *Phys. Rev. Lett.*, vol. 102, p. 073005, 2009.

[58] Q. Liu, L. Li, Y. Li, Z. Gao, Z. Chen, and J. Lu, "Tuning electronic structure of bilayer MoS_2 by vertical electric field: a first-principles investigation," *J. Phys. Chem. C*, vol. 116, pp. 21556–21562, 2012.

[59] L. Li, Y. Yu, G. J. Ye, Q. Ge, X. Ou, H. Wu, D. Feng, X. H. Chen, and Y. Zhang, "Black phosphorus field-effect transistors," *Nat. Nanotechnol.*, vol. 9, p. 372, 2014.

[60] E. S. Reich, "Phosphorene excites materials scientists," *Nature*, vol. 506, p. 19, 2014.

[61] Q. Wei and X. Peng, "Superior mechanical flexibility of phosphorene and few-layer black phosphorus," *Appl. Phys. Lett*, vol. 104, p. 251915, 2014.

[62] Y. Li, S. Yang, and J. Li, "Modulation of the electronic properties of ultrathin black phosphorus by strain and electrical field," *J. Phys. Chem. C*, vol. 118, pp. 23970–23976, 2014.

[63] J. Dai and X. C. Zeng, "Bilayer phosphorene: effect of stacking order on bandgap and its potential applications in thin-film solar cells," *J. Phys. Chem. Lett.*, vol. 5, pp. 1289–1293, 2014.

[64] A. S. Rodin, A. Carvalho, and A. H. C. Neto, "Strain-induced gap modification in black phosphorus," *Phys. Rev. Lett.*, vol. 112, p. 176801, 2014.

[65] Y. Liu, Z. Qiu, A. Carvalho, Y. Bao, H. Xu, S. J. R. Tan, W. Liu, A. H. Castro Neto, K. P. Loh, and J. Lu, "Gate-tunable giant Stark effect in few-layer black phosphorus," *Nano Lett.*, vol. 17, pp. 1970–1977, 2017.

[66] D. Li, J.-R. Xu, K. Ba, N. Xuan, M. Chen, Z. Sun, Y.-Z. Zhang, and Z. Zhang, "Tunable bandgap in few-layer black phosphorus by electrical field," *2D Mater.*, vol. 4, p. 031009, 2017.

[67] S.-L. Yan, Z.-J. Xie, J.-H. Chen, T. Taniguchi, and K. Watanabe, "Electrically tunable energy bandgap in dual-gated ultra-thin black phosphorus field effect transistors," *Chin. Phys. Lett*, vol. 34, p. 723, 2017.

[68] J. Kim, S. S. Baik, S. H. Ryu, Y. Sohn, S. Park, B.-G. Park, J. Denlinger, Y. Yi, H. J. Choi, and K. S. Kim, "Observation of tunable band gap and anisotropic Dirac semimetal state in black phosphorus," *Science*, vol. 349, p. 723, 2015.

[69] A. K. Singh and R. G. Hennig, "Computational prediction of two-dimensional group-IV mono-chalcogenides," *Appl. Phys. Lett*, vol. 105, p. 042103, 2014.

[70] J. P. Perdew, K. Burke, and M. Ernzerhof, "Generalized gradient approximation made simple," *Phys. Rev. lett.*, vol. 77, no. 18, p. 3865, 1996.

[71] F. Li, X. Liu, Y. Wang, and Y. Li, "Germanium monosulfide monolayer: a novel two-dimensional semiconductor with high carrier mobility," *J. Mater. Chem. C*, vol. 4, pp. 2155–2159, 2016.

[72] R. Fei, W. Li, J. Li, and L. Yang, "Giant piezoelectricity of monolayer group IV monochalcogenides: SnSe, SnS, GeSe, and GeS," *Appl. Phys. Lett*, vol. 107, p. 173104, 2015.

[73] A. Brown and S. Rundqvist, "Refinement of the crystal structure of black phosphorus," *Acta Crystallogr.*, vol. 19, p. 684, 1965.

[74] T. Grandke and L. Ley, "Angular-resolved uv photoemission and the band structure of GeS," *Phys. Rev. B*, vol. 16, no. 2, p. 832, 1977.

[75] H. C. Hsueh, M. C. Warren, H. Vass, G. J. Ackland, S. J. Clark, and J. Crain, "Vibrational properties of the layered semiconductor germanium sulfide under hydrostatic pressure: Theory and experiment," *Phys. Rev. B*, vol. 53, no. 22, p. 14806, 1996.

[76] H. C. Hsueh, H. Vass, S. J. Clark, G. J. Ackland, and J. Crain, "High-pressure effects in the layered semiconductor germanium selenide," *Phys. Rev. B*, vol. 51, no. 23, p. 16750, 1995.

[77] W. B. Pearson, *A Handbook of Lattice Spacings and Structures of Metals and Alloys*, vol. 3. London: Pergamon, 1 ed., 1958.

[78] L. Ehm, K. Knorr, P. Dera, A. Krimmel, P. Bouvier, and M. Mezouar, "Pressure-induced structural phase transition in the IV–VI semiconductor SnS," *J. Phys. Condens. Matter*, vol. 16, pp. 3545–3554, 2004.

[79] I. Lefebvre, M. A. Szymanski, J. Olivier-Fourcade, and J. C. Jumas, "Electronic structure of tin monochalcogenides from SnO to SnTe," *Phys. Rev. B*, vol. 58, no. 4, p. 1896, 1998.

[80] L. C. Gomes, A. Carvalho, and A. H. Castro Neto, "Enhanced piezoelectricity and modified dielectric screening of two-dimensional group-IV monochalcogenides," *Phys. Rev. B*, vol. 92, p. 214103, 2015.

[81] K.-A. N. Duerloo, M. T. Ong, and E. J. Reed, "Intrinsic piezoelectricity in two-dimensional materials," *J. Phys. Chem. Lett.*, vol. 3, pp. 2871–2876, 2012.

[82] L. Huang, F. Wu, and J. Li, "Structural anisotropy results in strain-tunable electronic and optical properties in monolayer GeX and SnX (X = S, Se, Te)," *J. Chem. Phys.*, vol. 144, p. 114708, 2016.

[83] H. Asahina and A. Morita, "Band structure and optical properties of black phosphorus," *J. Phys. C. Solid State Phys.*, vol. 17, p. 1839, 1984.